

Figure 5.37 Radial Displacement at Azimuth 135 degrees, Elev. 6200

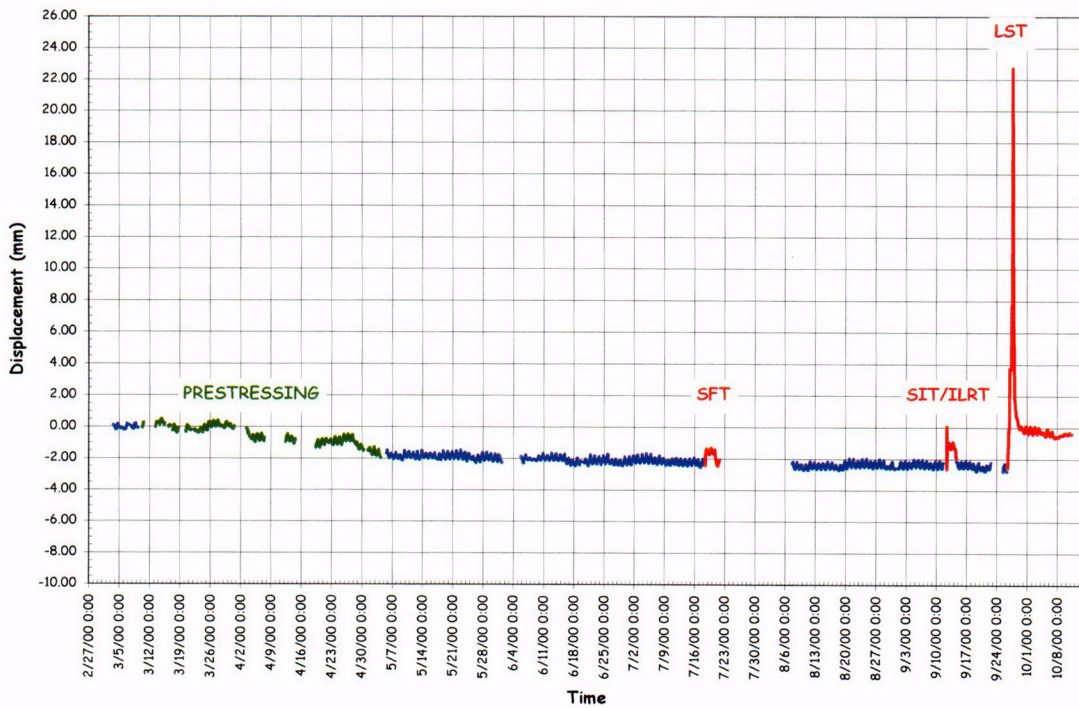


Figure 5.38 Radial Displacement History at Azimuth 135 degrees, Elev. 6200 (DT-R-Z6-01)

After the raw data was stored, it was converted using utility programs constructed as part of the DAS software. The conversion process was described in Chapter 4 and consisted of applying gage specific-gage factors (GFAC) obtained from the manufacturer or from gage calibration test data, correcting for actual gage power supply voltages. This converted data (CONV) was also stored as ASCII, tab-delimited text files (.dat) for each type of gage and loading period.

To simplify access to the data, the converted data files were further reorganized and stored in Microsoft Excel[®] spreadsheet format (.xls). The data files were grouped by response variable type according to the scheme shown in Table 5.3. Each data file was further subdivided by grouping similar gages on separate worksheets, as shown. Units for each response variable/gage are also shown. The converted data files in Excel[®] format are provided with this report on a CD. Appendix I provides a complete list of the data files on the disk. The format of each data file consists of the time (at the start of the data scan) in the first column followed by the response for each of the gages, identified by gage name in the following columns. The Excel[®] data files were also modified to add the average pressure at each time step where appropriate, (i.e., for the pressure tests), the nominal azimuth, elevation, and, in some cases, radius of the gage, and additional information (such as references to an instrumentation drawing detail or tendon number), where applicable.

The data file naming scheme consists of

- the gage type acronym,
- the data type acronym,
- a designation for dynamic (DYN) or DOR, and
- the loading period acronym.

For example, the file:

DISP_CVTD_DYN_LST.xls

contains the converted (CVTD) DYN displacement (DISP) during the LST in Excel[®] format (.xls).

One final set of data files, corrected data (COR), is also provided. The model was exposed to variations in ambient temperature, both temporal (day/night, seasonal) and spatial (due to direct solar heating), and responded accordingly. Since the converted test data includes the response to ambient thermal conditions, as well as prestressing and pressure loads, and the analyses, typically, do not, an attempt was made to correct the test data and 'remove' the effect of the temperature transient. This correction is described in Appendix J and was only applied to the LST data files.

In addition to the basic data files described above, additional data was collected by the pressurization system, acoustic system, and from visual observation and photographic (still and video records). This data is described in the following sections.

5.3.2 Limit State Test Results

5.3.2.1 Test Data

The LST data (DYN and DOR) is provided on the enclosed data CD in Excel[®] spreadsheets, as noted in Section 5.3.1. The response of every functioning transducer is provided. The following sections present a synthesis of the data focusing on the critical response measurements.

5.2.3.1.1 Displacements

The displacement data provides the most comprehensive view of the overall or global response of the model. Figures 5.39 through 5.42 show the displacement response as a function of pressure at various azimuths and elevations.

Table 5.3 Data File (Excel®) Format

Gage Type	Gage Type Acronym	Worksheet Label
Displacements	DISP	Unit: millimeters
		Radial
		Meridional
		Hatches
		Instrumentation Frame
Gage Bar Strains	GBST	Unit: strain
		Wall-Base 90 deg
		Wall-Base 135 deg
		Wall-Base 350 deg
		Above Tendon Gallery
Liner Strains	LINST	Unit: strain
		Free-Field Hoop
		Free-Field Merid
		Free-Field Merid Anchors
		E-H Details
		A-L Details
		M-S Details
		F-W Details
		Wall-Base
		Misc Details
Pressure	PRES	Unit: MegaPascal
Rebar Strain	REBST	Unit: strain
		Free-Field Hoop
		Free-Field Merid
		Free-Field Radial Bar
		Basemat
		E-H Bars
		A-L Bars
Temperature	TEMP	Unit: °Celsius
		Inside Air (includes outside air temperature)
		Inside Liner
		Embedded Concrete
Tendons	TENDON	Unit: Newtons/strain
		Load Cells (grouped by tendon)
		Tensmegs (grouped by tendon)
		Strain Gages (grouped by tendon)
Concrete Strain*	SOFO*	Unit: strain

*Concrete strains by SOFO gages were only measured during prestressing and pressure tests.

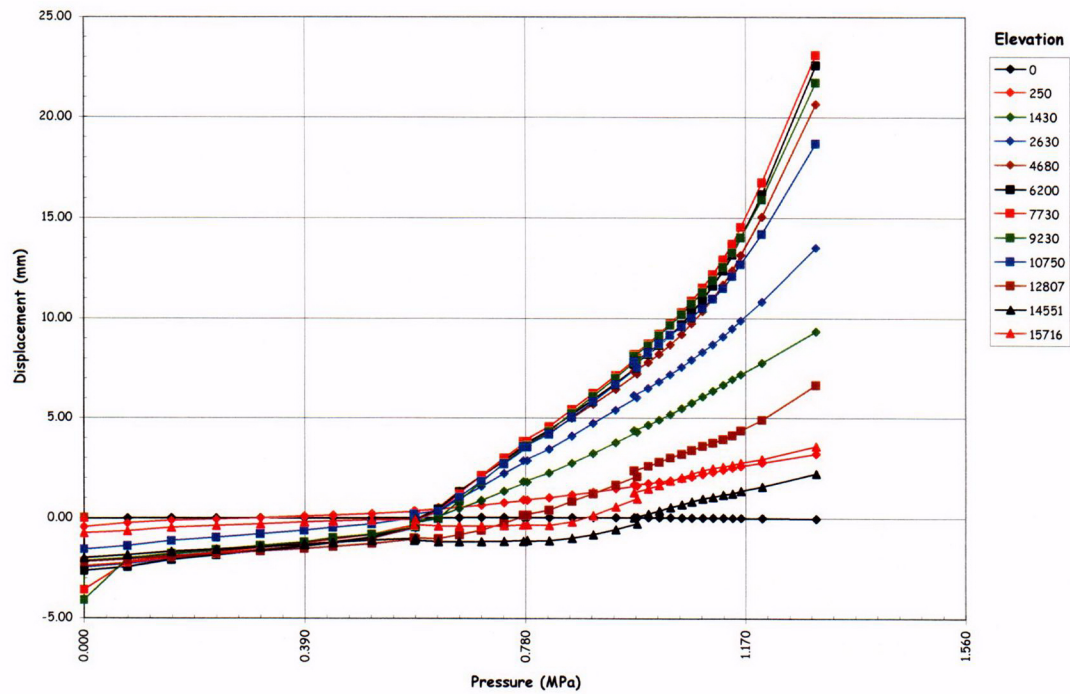


Figure 5.39 LST - Radial Displacement at Azimuth 135 degrees

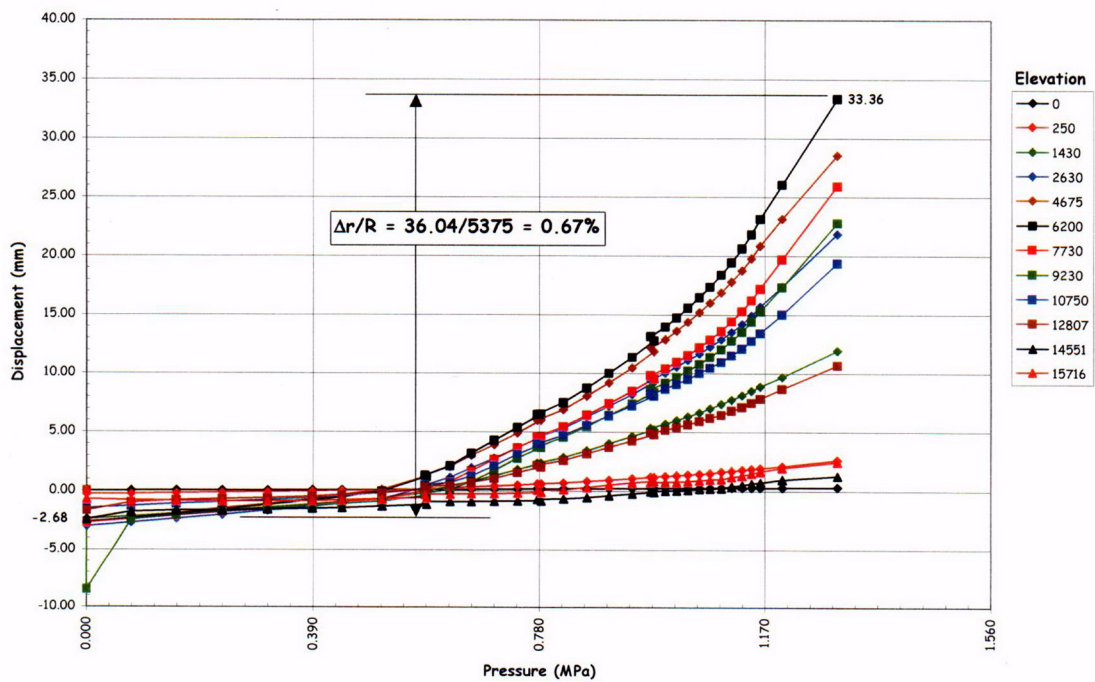


Figure 5.40 LST - Radial Displacement at Azimuth 324 degrees

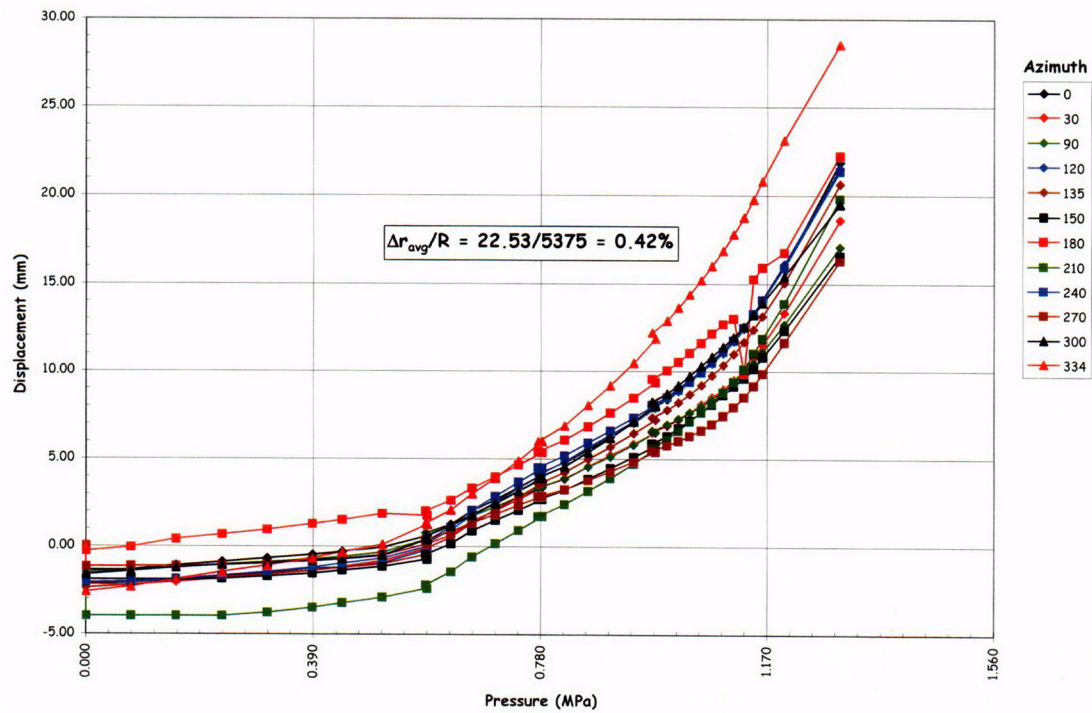


Figure 5.41 LST-Radial Displacement (DOR) at EL 4680

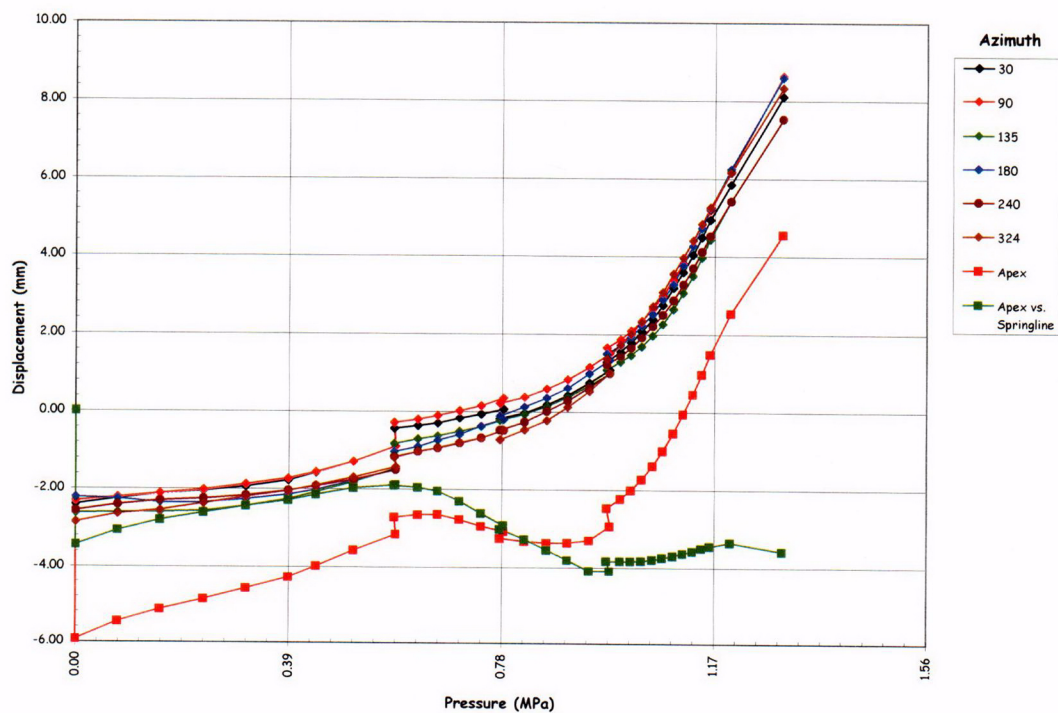


Figure 5.42 LST-Vertical Displacements (DOR) at Springline, El. 10750

The radial displacement of the model at the cardinal elevations along Azimuth 135 degrees, selected to represent the 'free-field' or axisymmetric response of the model, is shown in Figure 5.39. This plot illustrates several features of the response data that should be noted. The initial values (i.e. at $P=0$) reflect the inside surface motion of the liner between March 3rd and the start of the LST, thereby reflecting the influence of prestressing, changes in ambient temperature, creep, etc. The response due to pressure alone is the reported displacement minus the displacement at the start of the LST (i.e., at $P=0$ on 10:03 a.m., 26 September, 2000).

The initial data also suggests that the liner most likely separated from the concrete wall at some locations, as evidenced by the relatively large displacements that occurred during the first pressure step. At these locations, the first increment of pressure 'pushed' the liner back into contact with the concrete surface. This behavior can also be observed in the SFT and SIT/ILRT data, including a restoration of the gap after depressurization. The liner separation is most likely a result of differential thermal expansion and prestressing, resulting in compressive stresses that may have bowed or slightly buckled the liner.

The response remains essentially elastic up to 1.3 to $1.5 P_d$, after overcoming the prestress ($\sim 1.2 P_d$) and tensile cracking of the concrete. It is interesting to note that even though drying and shrinkage cracks were present prior to pressure testing, the onset of generalized concrete tensile cracking is quite distinct. Beyond $1.5 P_d$ to approximately 2 to $2.5 P_d$, the response is still linear, although the loss of concrete tensile stiffness is quite distinct. Beyond $2.5 P_d$, the response becomes increasingly nonlinear, particularly in the mid-section of the cylinder, as the model exhibits generalized yielding in the hoop direction.

The data also exhibits some apparent discontinuities at 1.5 , 2.0 , and $2.5 P_d$. These apparent discontinuities coincide with the leak checks of the model and reflect, primarily, the response to changes in ambient thermal conditions over the time the model was isolated. The jump in displacement at $2.5 P_d$, however, most likely includes creep effects, since the temperature was stable over the relatively short (1-1/2 hour) hold at this pressure.

Figure 5.40 displays the displacements at Azimuth 324 degrees, which coincides with the centerline of the E/H. The largest radial displacement recorded during the LST, 33.36 mm, occurred at this Azimuth at El. 6200, above the E/H. Computing the equivalent hoop strain due to pressure at this location from kinematics,

$$@P_{\max} = \frac{\Delta r}{R} = \frac{(33.36 + 2.68)}{5375} = 0.67\%$$

Similarly, calculating the local hoop strain in the vicinity of the equipment hatch at $2.5 P_d$, corresponding with the onset of liner tearing and leakage, yields a value of approximately 0.28% .

Figure 5.40 again illustrates the liner separation phenomena, previously described, at elev. 9230. In this case the large magnitude of the displacement clearly indicates that the liner buckled. (A review of the post-prestressing data indicates that this occurred shortly after the completion of prestressing, most likely in conjunction with thermally-induced compressive strains.) This behavior did not, however, compromise the integrity of the liner and no tears were discovered at this location.

Figure 5.41 compares the displacement response as a function of Azimuth at elev. 4680, nominally the mid-height of the cylinder and the centerline of the E/H, A/L, and M/S penetrations. Ignoring some variation in initial conditions, reflecting some 'out-of-roundness' following prestressing, the response is fairly uniform, i.e. axisymmetric, except at 324 degrees, where largest deflections were already noted to occur. Averaging the radial deformation due to pressure yields a nominal average hoop strain of 0.42% at the peak pressure $3.3 P_d$. Similarly, the average hoop strain at $2.5 P_d$, coinciding with the onset of liner tearing and leakage, was 0.18% .

Figure 5.42 shows the vertical displacement of the springline at various azimuths. The vertical displacement at the apex and the differential displacement between the average springline displacement and the apex are also plotted. The vertical displacement exhibits similar behavior to the hoop displacements. In the vertical direction, however, the loss of stiffness due to concrete cracking occurs around $2.5 P_d$. Yielding in the vertical direction does not appear to occur. This is due to the higher level of vertical prestress in the cylinder wall and the lower tensile forces induced by the pressure. The

vertical displacement is nearly uniform at the springline and the average meridional strain in the cylinder wall is less than 0.1%.

$$@P_{\max} = 3.3P_d; \quad \frac{\Delta l}{L} = \frac{(8.00 + 2.50)}{10750} = 0.10\%$$

The vertical displacements illustrate, much more dramatically, the effect of ambient temperature and creep during the leak checks.

Figure 5.42 also shows that beginning around $1.5P_d$, the dome apex deflects downward relative to the springline, most likely due to increasing force in the vertical tendons once the initial prestressing force is overcome by the pressure. (The vertical prestressing applies a compressive force on the cylinder wall approximately equal to the tensile force exerted by a pressure of $1.88P_d$.)

Deformed profiles of the PCCV model, constructed from the displacement data, are shown in Figures 5.43 through 5.45. These figures provide a more illuminating view of the model behavior than the pressure histories. The figures were constructed by applying the displacement data (exaggerated by a factor of 100) to the initial configuration of the model. The initial conditions were defined by the as-built model survey data (Appendix C). While these measurements were made in July, 1999, it was assumed that any changes in the position of the cardinal points by March, 2000 could be neglected without significant error. The motion of the cardinal points without displacement transducers were computed by linear interpolation. Both radial and vertical displacements were applied to the cardinal points and out-of-plane (i.e. circumferential) motion of the was not measured or considered.

The as-built position of the PCCV model is plotted along with the deformed shapes at the start of the LST ($P = 0$), at approximately $1.0P_d$ (0.398 MPa/57 psi), $2.0 P_d$ (0.776 MPa/113 psi), $2.5 P_d$ (0.978 MPa/142 psi), $3.0 P_d$ (1.162 MPa/169 psi), and $3.3 P_d$ (1.295 MPa/188 psi).

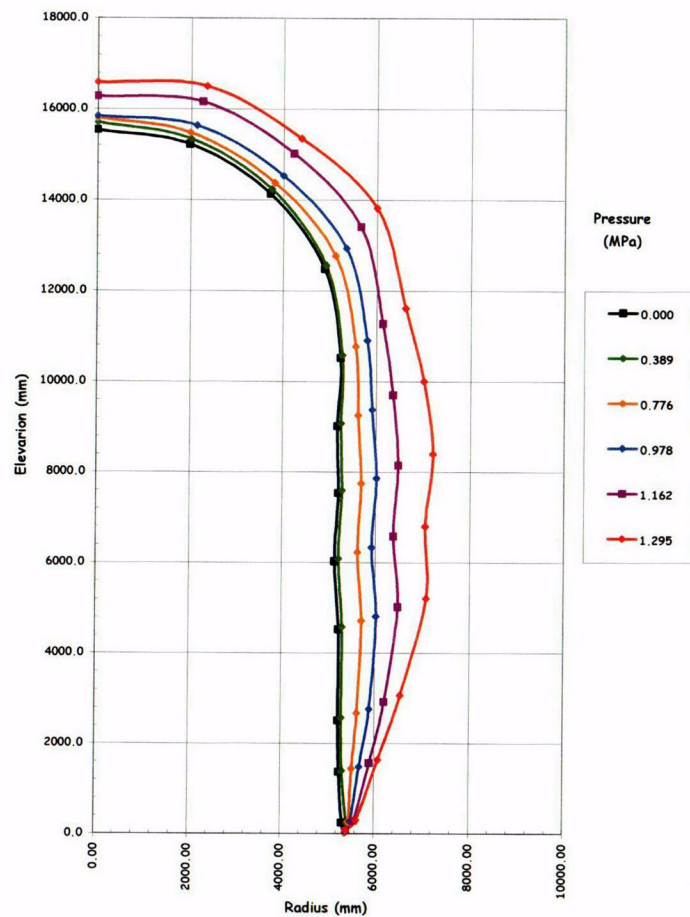
The figures illustrate a few interesting points about the behavior of the PCCV model.

First, and most importantly, the radial deformations are smallest at the buttresses (90 degrees and 270 degrees) and larger between the buttresses (0 degrees and 180 degrees), illustrating the stiffening effect of the buttresses even though the net hoop prestressing force is smallest at the buttress. The largest radial deformations are at the E/H and A/L penetrations, showing the reduced stiffness of these regions in spite of thickening and added conventional reinforcing. This reduction in stiffness is due to the lower prestressing forces as the tendons are deflected around the penetrations in addition to the opening itself.

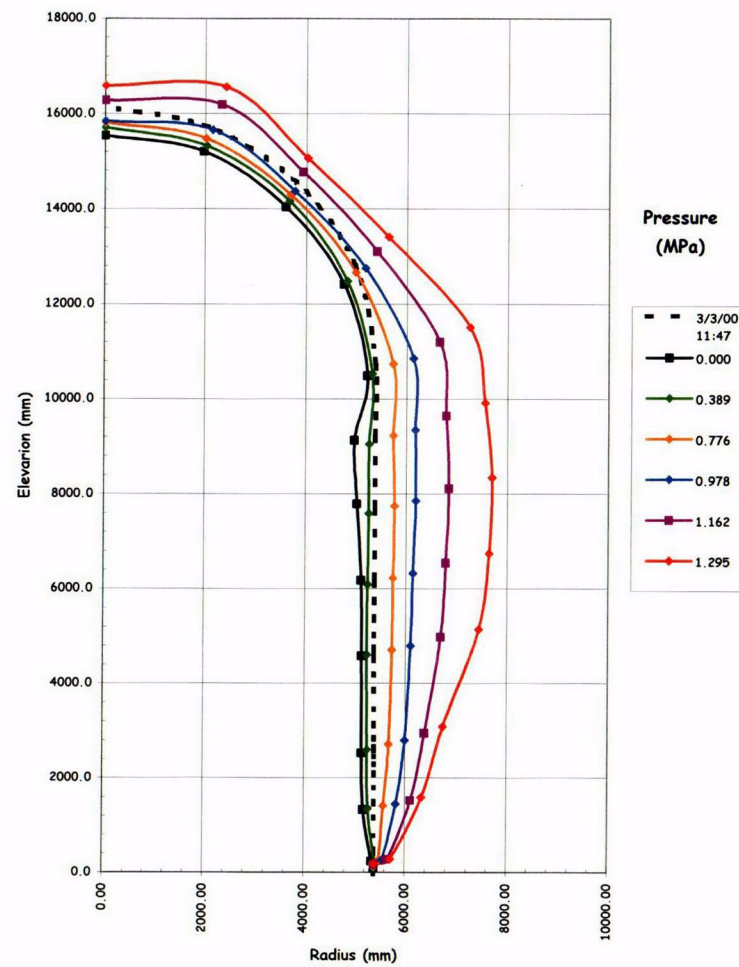
Secondly, the vertical profiles do not show any reverse curvature at the wall-base junction and seem to imply the presence of a hinge forming at this location. While a hinge may have occurred, this deformation pattern may be more reflective of an instrumentation artifact than the model's behavior in this region. The displacement transducers at the wall-base junction were anchored to the base liner immediately adjacent to the wall, while the displacements above this point were measure relative to the instrumentation frame. It is likely that the differential displacement measured at the wall-base junction does not accurately reflect the total displacement in this region, and the data should be viewed with this limitation in mind.

Finally, a few other minor observations:

- The unusual deformation patten in the dome at 135 degrees and 324 degrees coincides with the regions where the East-West and North-South sets of vertical tendons overlap with the hoop tendons in the dome, where higher prestressing forces are present than in other regions of the dome.
- The initial buckling of the liner at Azimuth 324 degrees, elev. 9230 is clearly shown in Figure 5.44.

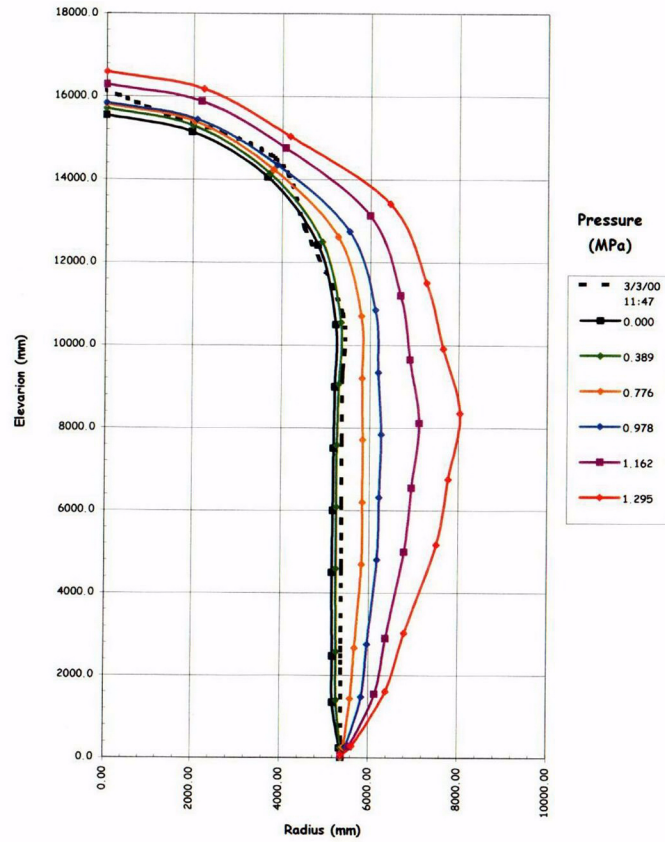


(90°)

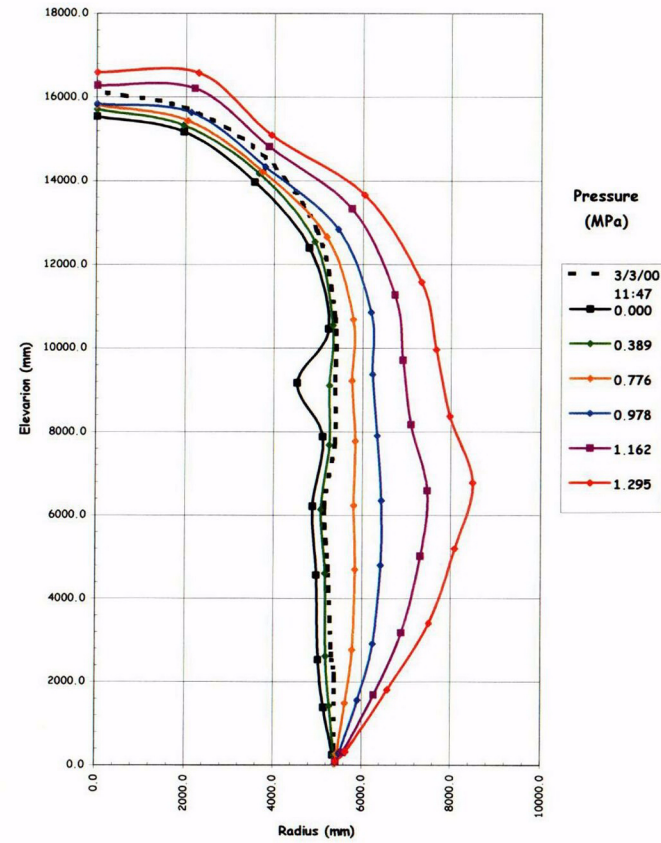


(135°)

Figure 5.43 LST - Deformation at Azimuth 90 degrees and 135 degrees (D and Z) $\times 100$



(240°)



(324°)

Figure 5.44 LST - Deformation at Azimuth 240 degrees and 324 degrees (I and L) $\times 100$

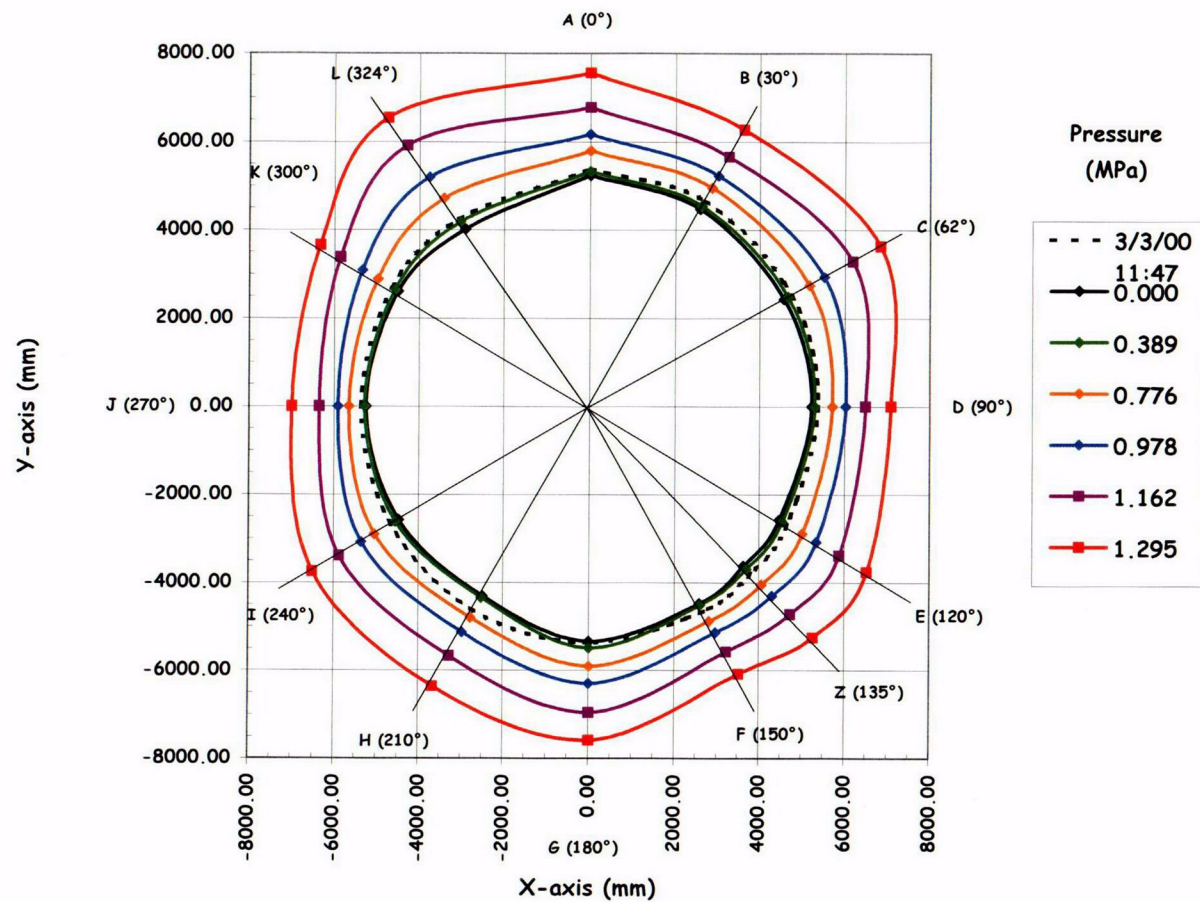


Figure 5.45 LST - Deformation at Elev. 4680 (5) \times 100

5.3.2.1.2 Liner Strains

Five hundred and fifty-nine strain gages were placed on both surfaces of the liner to measure both the meridional and hoop free-field liner strains, as well as local strains at the penetrations, the wall-base junction, liner anchor, and stiffeners where discontinuities might result in high local strains prior to the liner tearing. The data for each of these gages is provided on the enclosed CD. The majority of these gages did not record significant strains, however, gages at a number of locations deserve closer inspection. Table 5.4 summarizes the maximum strains recorded during the LST at locations of interest.

Before considering several of these locations in detail, it is worth noting that individual strain gages can provide misleading information due to their sensitivity to local as-built conditions, particularly in areas of sharp discontinuities and high strain gradients. As a result, it is more meaningful to consider sets of gages in these locations, thus providing a more realistic view of the strain field in a particular area.

Figure 5.46 shows all the free-field liner hoop strain gages that exceeded 0.5% at the end of the test. It is interesting to note that up to 2.5 Pd, the free-field liner strain hoop strains were almost all below 0.2%, which compares favorably with the average hoop strain computed from the displacements, 0.18%.

Nearly all the free-field liner and liner anchor meridional strain gages were below 0.1%, which is also consistent with the displacement data.

Considering the liner strains near penetrations and other discontinuities, the strains in the vicinity of the E/H are of primary interest since there were indications during the LST that the liner initially tore in this region. Posttest inspection of the liner, described in Section 5.3.2.2, revealed several tears at the edges of the embossment (Figure 5.47), but no apparent damage near the insert plate. The layout of the liner strain gages is shown on Drawing D-SN-P-218 (Appendix E), and reproduced in Figure 5.48 for reference. The highest strains in this region were at the left and right edges of the embossment. The strains adjacent to the insert plate (#19 to #67) were small, nearly all less than 0.2% at maximum pressure, with only a few near the ends of anchors or stiffeners reaching 0.5%.

Table 5.4 LST Liner Strain Summary

Maximum Free-Field Hoop Strain	0.90%
Maximum Free-Field Meridional Strain	0.14%
Maximum Meridional Anchor Strain	0.10%
Maximum Equipment Hatch Strain	3.88%
Maximum Personnel Airlock Strain	0.75%
Maximum Main Steam Penetration Strain	4.54%
Maximum Feedwater Penetration Strain	6.39%
Maximum Wall-Base Junction Strain	1.97%
Maximum Miscellaneous Liner Details Strain	5.75%

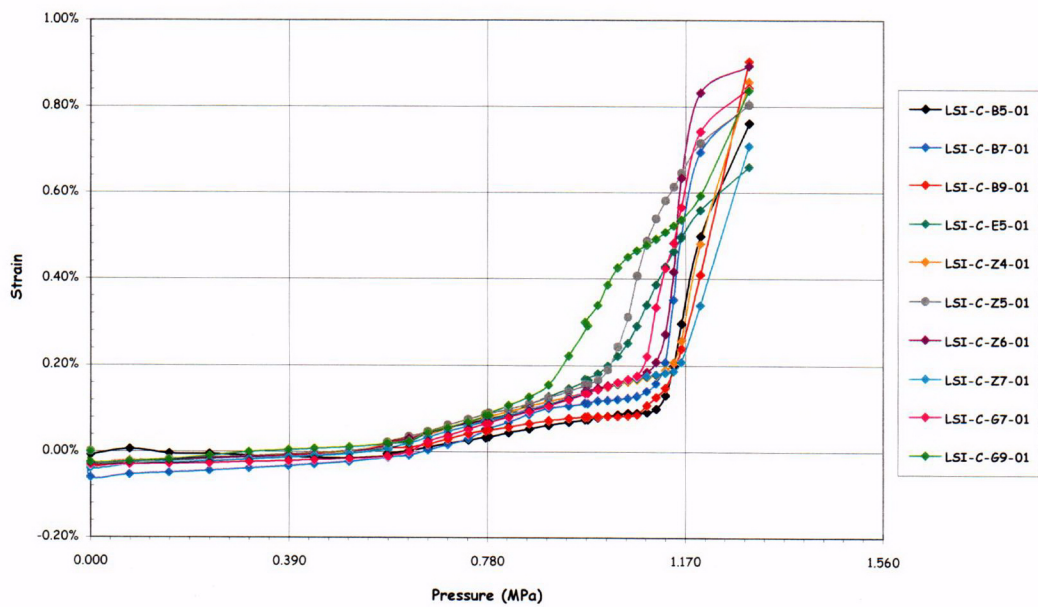


Figure 5.46 LST – Free-Field Liner Hoop Strains

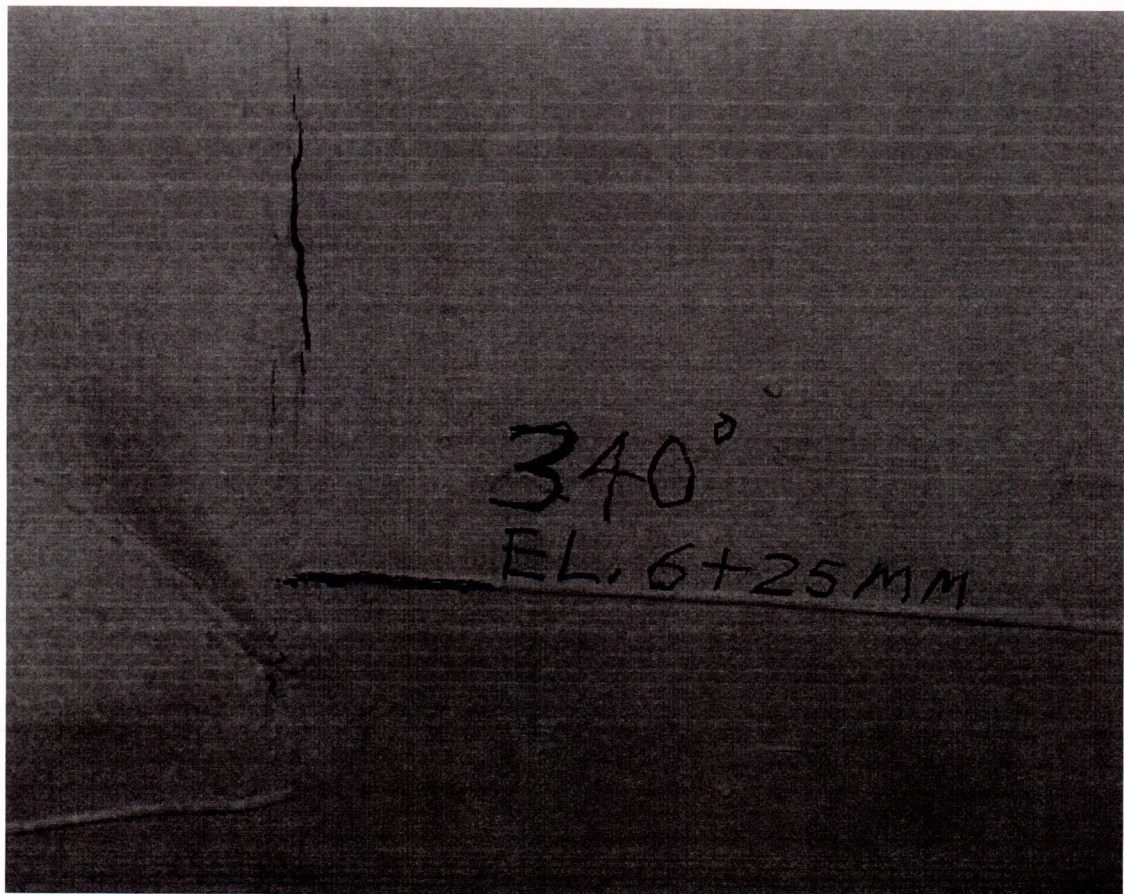


Figure 5.47 Liner Tear (#15) at E/H

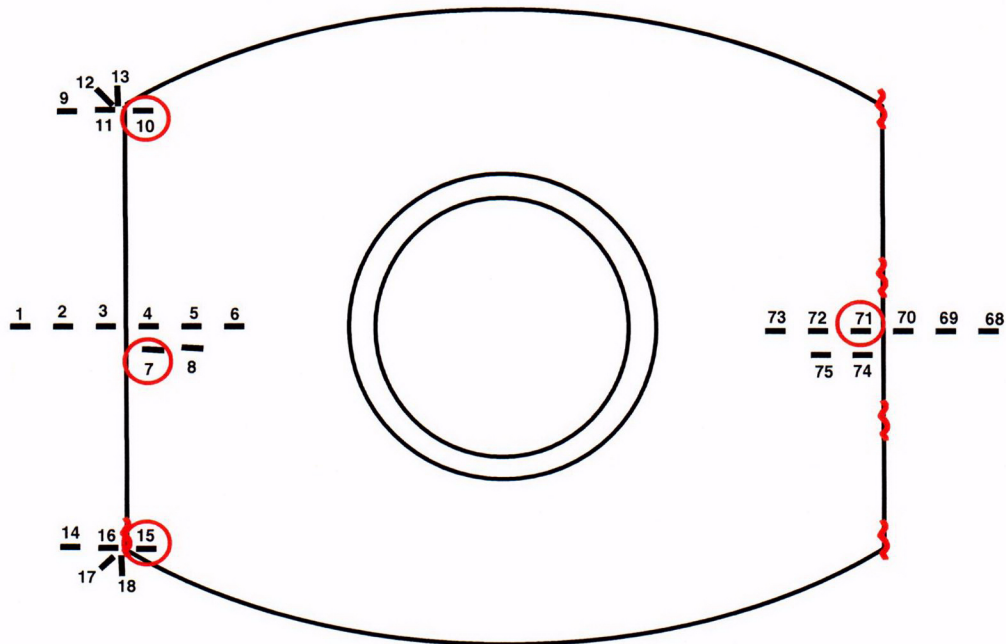


Figure 5.48 Equipment Hatch Liner Strain Gage Layout (Inside View)

The strains at the middle of the 'left' (#1-8) and right (#68-75) edges of the embossment are shown in Figures 5.49 and 5.50. The strains at the upper and lower 'left' corners are shown in Figure 5.51. With the exception of gage #7, the strains at the mid-sides of the embossment are all very small until global yielding of the model occurs just below $3P_d$. At the corners, however, liner strains begin increasing earlier, with gage #10 showing increasing strains beginning at $1.5P_d$, while most of the other gages show significant increases beginning at $2.5P_d$, when liner tearing was believed to

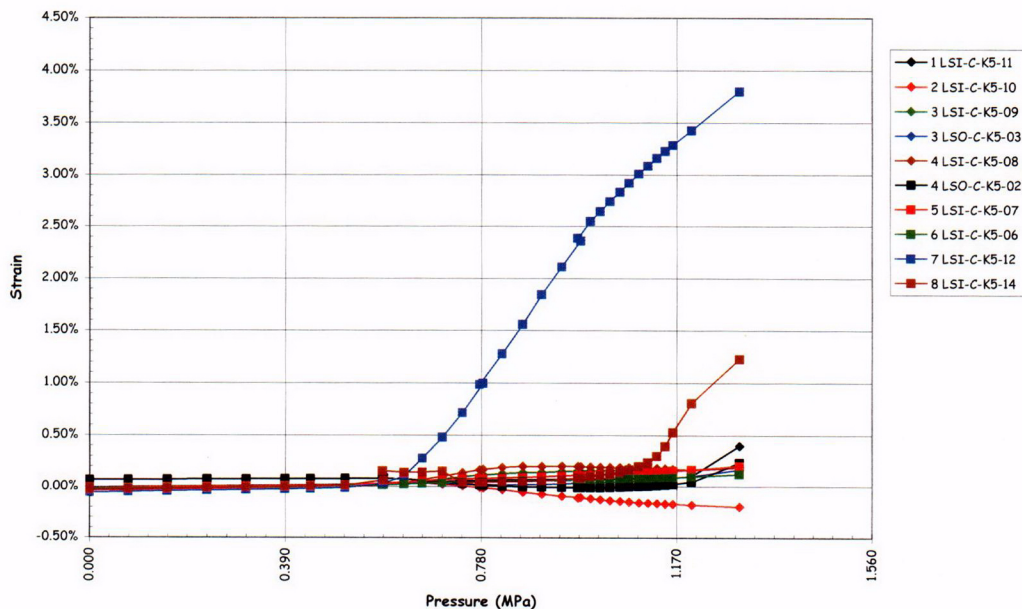


Figure 5.49 E/H Liner Strains at 'Left' Edge of Embossment

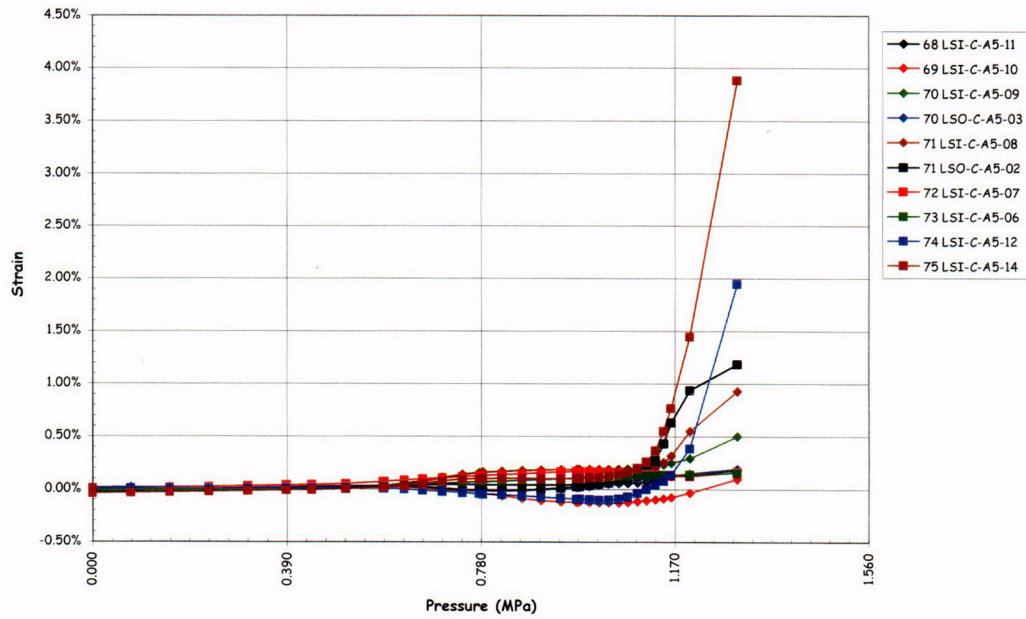


Figure 5.50 E/H Liner Strains at 'Right' Edge of Embossment

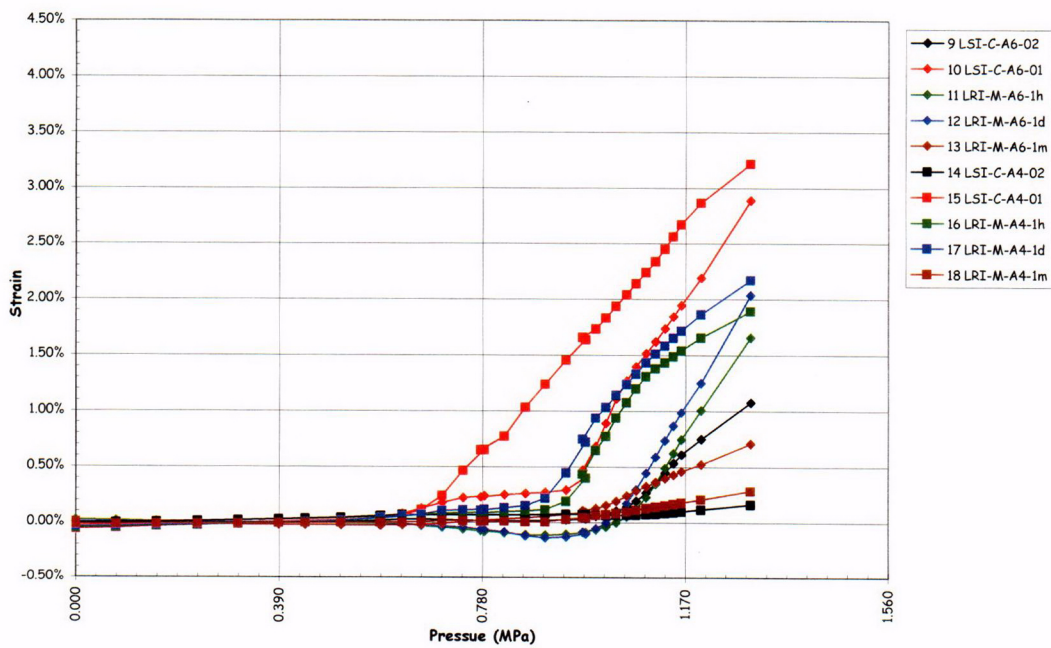


Figure 5.51 E/H Liner Strains at 'Left' Corners of Embossment

have occurred. At first glance, it appears unfortunate that the liner tore on the opposite side from the strain gages (pretest analyses suggested the highest strains would occur on the 'left' side). However, it has been found that strain gages near tears often see lower strains than would be expected, since the tear acts as a strain relief mechanism. While it is apparent that the strains on the 'right' side were higher, it is unlikely that gages at those locations would have recorded higher strains than those on the left side. This is demonstrated by comparing gages #7 on the left and its mirror image, #74, on the right.

Note that at the pressure $2.5 P_d$, when the liner tearing is believed to have begun, the measured strains were only on the order of 0.75% to 1.50%.

The liner strain at the A/L shows a similar pattern to those at the E/H, with a peak tensile strain at the corner of the embossment of 0.75%. However, no tears occurred at this penetration.

Liner strains at the M/S and F/W penetrations are shown in Figures 5.52 and 5.53. The layout of the liner strain gages is shown on Drawing D-SN-P-220 (Appendix E).

Several large tears occurred at each end of the F/W penetration, beginning at the weld between the thickened insert plate and the liner; however, no tears occurred at the M/S penetration event, though the free-field hoop strains at the M/S are higher since it is closer to the mid-height of the cylinder. There are a number of reasons why this occurred, primarily liner fabrication issues discussed in Section 5.3.2.2. It is interesting to note that even though the strain gages at the F/W penetration were located near the tear (see Figure 5.54), measured strains were relatively low until the very end of the LST, when some strains increased very rapidly. This might indicate that a tear in the vicinity of a strain gage can act as a strain relief mechanism on the surrounding material. The 'jump' in the strain near the end of the test may also be due to material distortion in the vicinity of the tear as the tear propagated. On the other hand, the strains recorded at the M/S penetration begin to climb rapidly at 2.0 to $2.5 P_d$, reaching values as high as 4.5% without resulting in any liner tearing. Detailed inspections of this location did not reveal any evidence of the fabrication problems that were present at the F/W penetration.

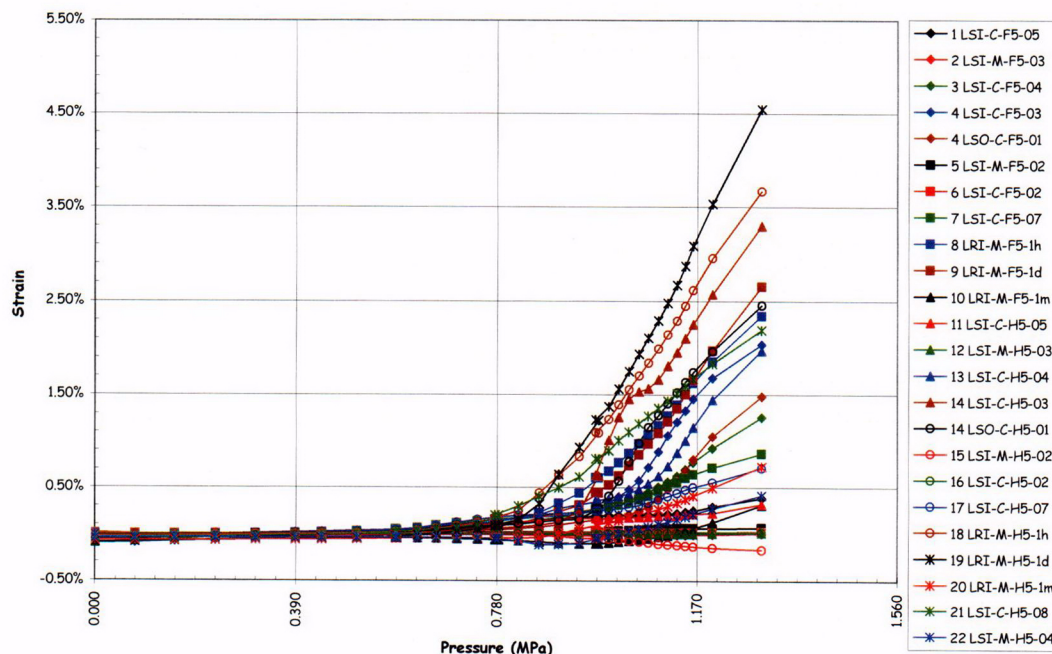


Figure 5.52 Liner Strains (DOR) at M/S (Ref. D-SN-P-220)

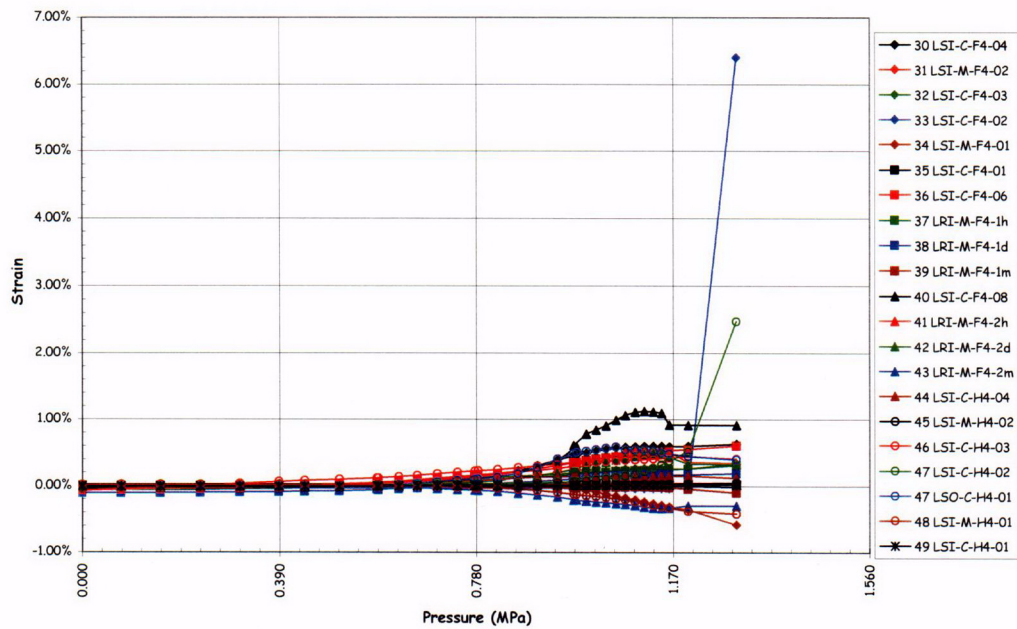


Figure 5.53 Liner Strains (DOR) at F/W (F=Ref. D-SN-P-220)

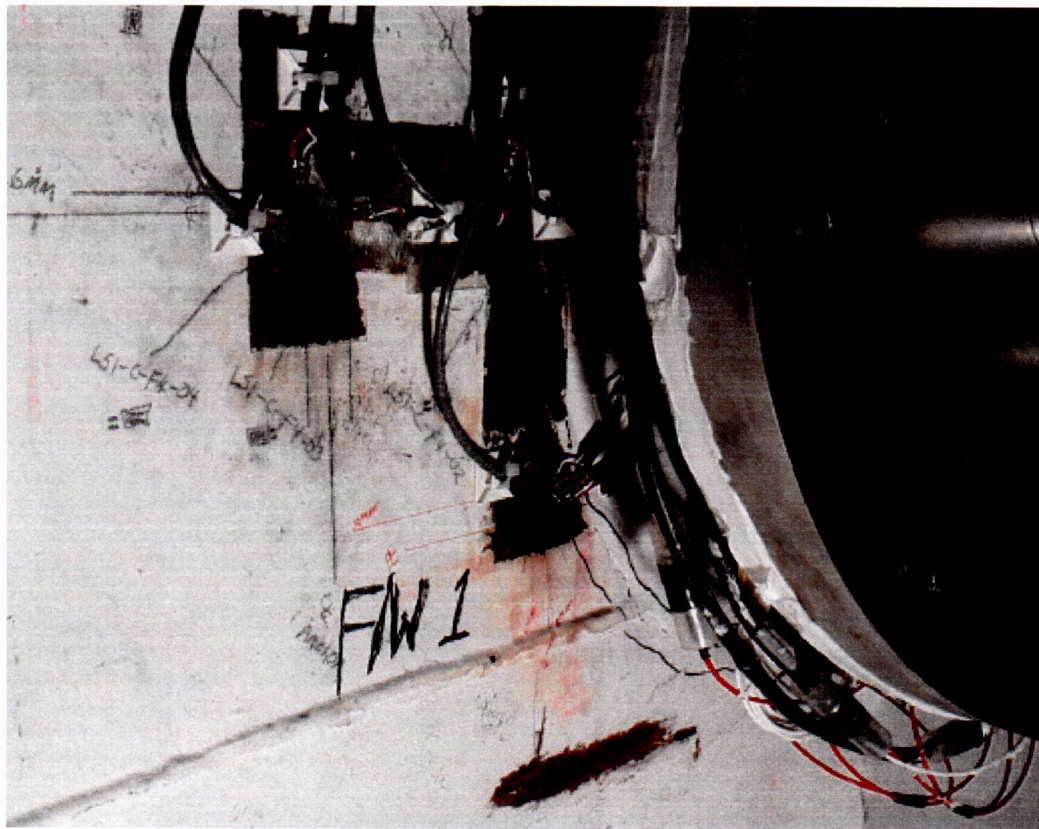


Figure 5.54 Liner Tear (#3) and Strain Gages at F/W Penetration

A number of other details believed to create potential strain concentrations in the liner were also instrumented and monitored during the test. One of these details occurs throughout the model: a gap is left in a horizontal stiffener or vertical anchor where it crosses a liner seam wells (Figure 5.55), euphemistically called a 'rathole.' In previous containment model tests, this detail caused significant strain concentrations when the surrounding liner began to yield. In fact, a number of the liner tears found after the test occurred at these details. One such detail that was instrumented was located near the intersection of cardinal lines D7 (Azimuth 90 degrees, elev. 7730). Although a tear occurred in a similar detail above this location, the liner did not tear at this rathole and the strains recorded at this location provided valuable information regarding the behavior of this detail for comparison with analyses.

The interior strain gages at D7 are also shown after the LST in Figure 5.56. The arrangement of these gages is shown on Drawing D-SN-P-209, Detail a.4 (Appendix E). Strains begin increasing between 2.0 and 2.5Pd, reaching a maximum of 5.7% at the maximum pressure. Nevertheless, the liner did not tear. A subsequent comparison of this detail to similar rathole details that did tear, but were not instrumented, revealed a lack of any weld repairs, which was not true of the other locations. This detail appears to demonstrate that the liner is capable of undergoing significant local strain without tearing in the absence of any other factors that might degrade the liner.

5.3.2.1.3 Rebar and Concrete Strains

The reinforcing steel strains are summarized in Table 5.5. Typically, after the onset of global yielding, the rebar strains were higher than the corresponding strains computed from displacements and the free-field liner strains. This phenomena was recognized during gage calibration and occurs due to a local reduction in cross-section from grinding away a portion of the bar to mount the strain gage. The effect of this local cross-section reduction causes the bar to yield at the gage location slightly before the rest of the bar yields. The effect on the rebar strain readings is to introduce an artificial strain increment, on the order of 0.5% strain, after the bar has yielded, compared to the strain that would occur if the gage were not present. This artifact can be illustrated by considering the hoop strain measurements at Z6 shown in Figure 5.57. Attempts were made to develop an algorithm to correct for this gage artifact; however, the results were not particularly useful. The rebar strain data included on the data CD were not corrected for this artifact, which any interpretation of this data should consider.

Figure 5.57 compares the hoop strains recorded at the mid-height of the cylinder wall (Z6: Azimuth 135 degrees, elev. 6280) by the fiber optic gages (CE), rebar strain gages (RS), liner strain gage (LI) and computed from the displacement (DT). The strains track each other very well until local yielding occurs in the liner and, shortly after, in the rebar. The fiber optic gage continues to track the displacement and provides a much more accurate measure of the hoop strain in the wall than the LI or RS gages.



Figure 5.55 Horizontal Stiffener Detail at Vertical Seam Weld ('Rathole') near D7

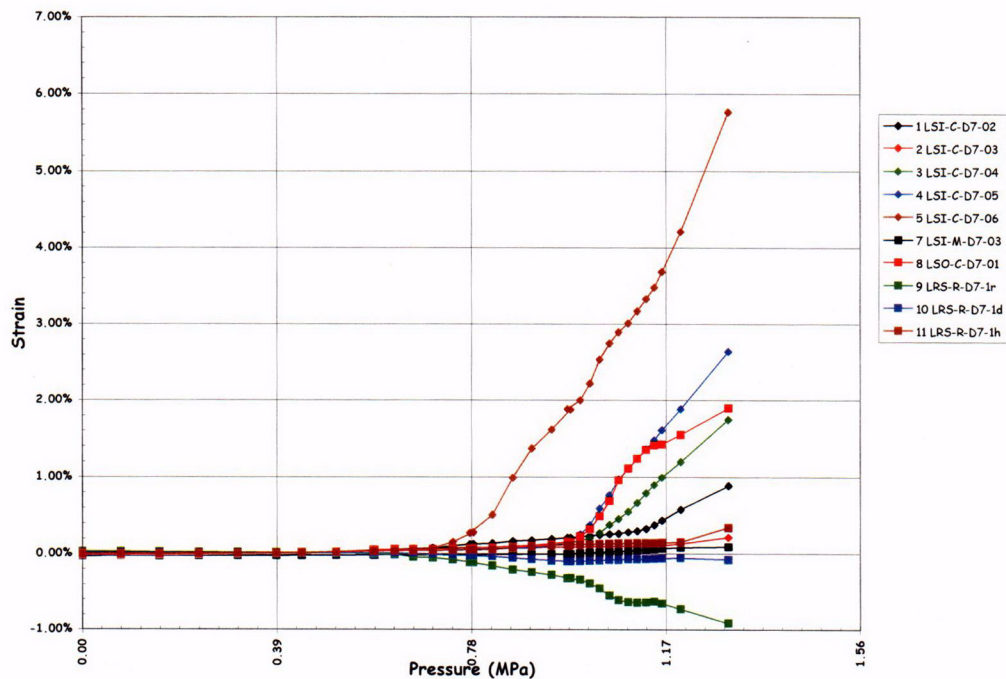


Figure 5.56 Liner Strains (DOR) at D7 Anchor Detail (Ref. R-SN-P-209, a.4)

Table 5.5 Rebar Strain Summary

Maximum Free Field Hoop Rebar Strain	1.68%
Maximum Free Field Meridional Rebar Strain*	0.47%
Maximum Free Field Radial Rebar Strain	0.88%
Maximum Basemat Rebar Strain	0.84%
Maximum Rebar Strain at E/H	1.62%
Maximum Rebar Strain at A/L	1.50%

* One gage (RS-M-A0-07) recorded a maximum strain of 6.11%. However, the initial strain of the start of the LST was 5.85%, yielding a change in strain of 0.27%. The initial high strain reading was due to an increase in resistance not associated with strain of the bar.

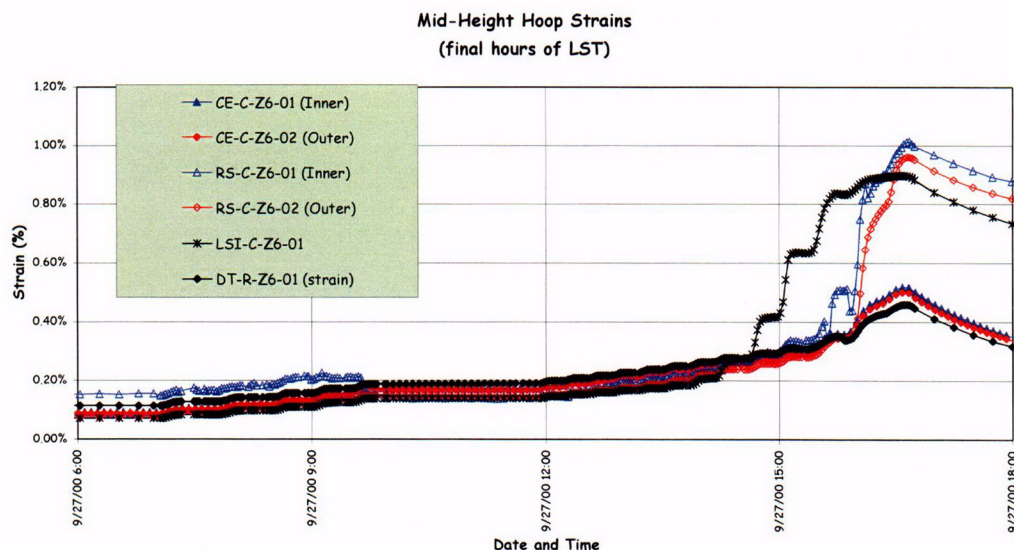


Figure 5.57 Comparison of Strain at Z6 (Azimuth 135 degrees, Elev. 6280)

Strain gages were also installed on specially fabricated 'gage bars,' which were located at several azimuths (90 degrees, 135 degrees and 350 degrees) at the wall-base junction in an attempt to get a more accurate picture of the strain fields at this location due to the presence of large bending forces under pressure (Figure 5.58). Unfortunately, a large number of these gages were damaged during construction and only very limited data was obtained. (Since the gage bars were embedded in the basemat, they were placed at the time of the final basemat lift and left exposed for almost two years until the first cylinder wall lift was placed. During this time, they were exposed to the weather and some rough handling by the construction workers.) However, enough gages survived at 135 degrees that it is possible to construct a picture of the strain history at this location. Figure 5.59 shows the distribution of strain *due to pressure only* at four elevations (86, 201, 312, and 427) above the top of the basemat. Only the strain due to pressure is plotted, since the initial strains due to dead load and prestressing are somewhat ambiguous and mask the pressure response. The strains recorded by the surviving gages at each elevation are plotted at pressure levels corresponding to $1P_d$, $2P_d$, $2.5P_d$, $3P_d$, and $3.3P_d$. While these results are incomplete, they do show the increasing curvature of the cross-section as a function of pressure, especially at elev. 427.

Some gage bars were also located in the basemat, above the tendon gallery, in an attempt to measure tensile strains that might develop at this location. However, there was no indication of any damage in this region and, with a few ambiguous exceptions, the gages did not record any response to the pressure loads.

Overall, in spite of the significant effort (and expense) involved in the application and installation of the rebar strain gages, the resulting data is only marginally useful and any future tests of a similar nature would be advised to consider the method of installing strain gages on rebar and to limit the number of gages to a few, critical locations.

5.3.2.1.4 Tendon Forces and Strains

Since the unique feature of this model, compared to previous large-scale containment models tested at SNL, is the prestressing system, and the behavior of this system to pressure loads beyond design levels is of particular interest, a significant effort was made to measure the response of the tendons. Both tendon anchor forces, as well as strains along the length of the tendons, were measured. Unfortunately, as noted in Chapter 2, approximately 50% of the strain gages installed on the tendons strands were damaged during construction and/or prestressing. Furthermore, data from the Tensmeg gages indicates the likelihood that these gages de-bonded or slipped relative to the tendon strands, casting some doubt on the accuracy of the data.

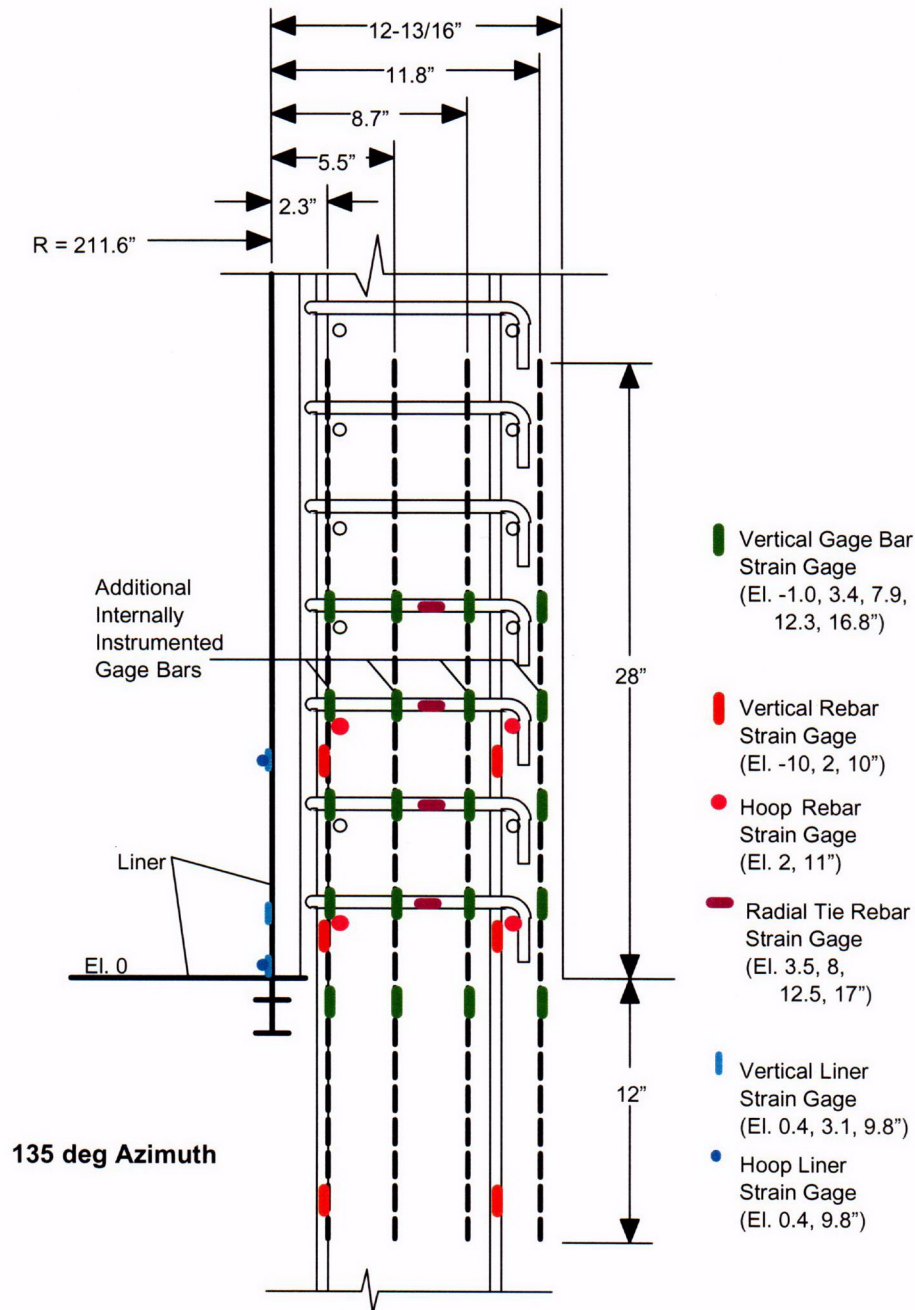


Figure 5.58 Arrangement of Gage Bar Strain Gages at Azimuth 135 degrees

Nevertheless, the surviving gages provide some significant insight into the response of the tendons to the pressure loading. All of the tendon data (load cells and strain gages) is provided on the enclosed CD, as described in Section 5.3.1. A summary of the data and a discussion of the LST results follows.

One-sixth of the tendons in the model were equipped with load cells at each anchor prior to prestressing. Figures 5.60 through 5.62 illustrate the tendon anchor forces during the LST. The anchor forces for the vertical tendons with load cells are shown in Figure 5.60. The anchor forces are shown for the maximum tensioning force during prestressing, after the completion of prestressing (on 5/4/00) and during the LST at $0.0P_d$, $1.0P_d$, $2.0P_d$, $2.5P_d$, $3.0P_d$ and at maximum pressure, $3.3P_d$. Similarly, Figures 5.61 and 5.62 show the anchor forces for the hoop tendons anchored at the 90 degree

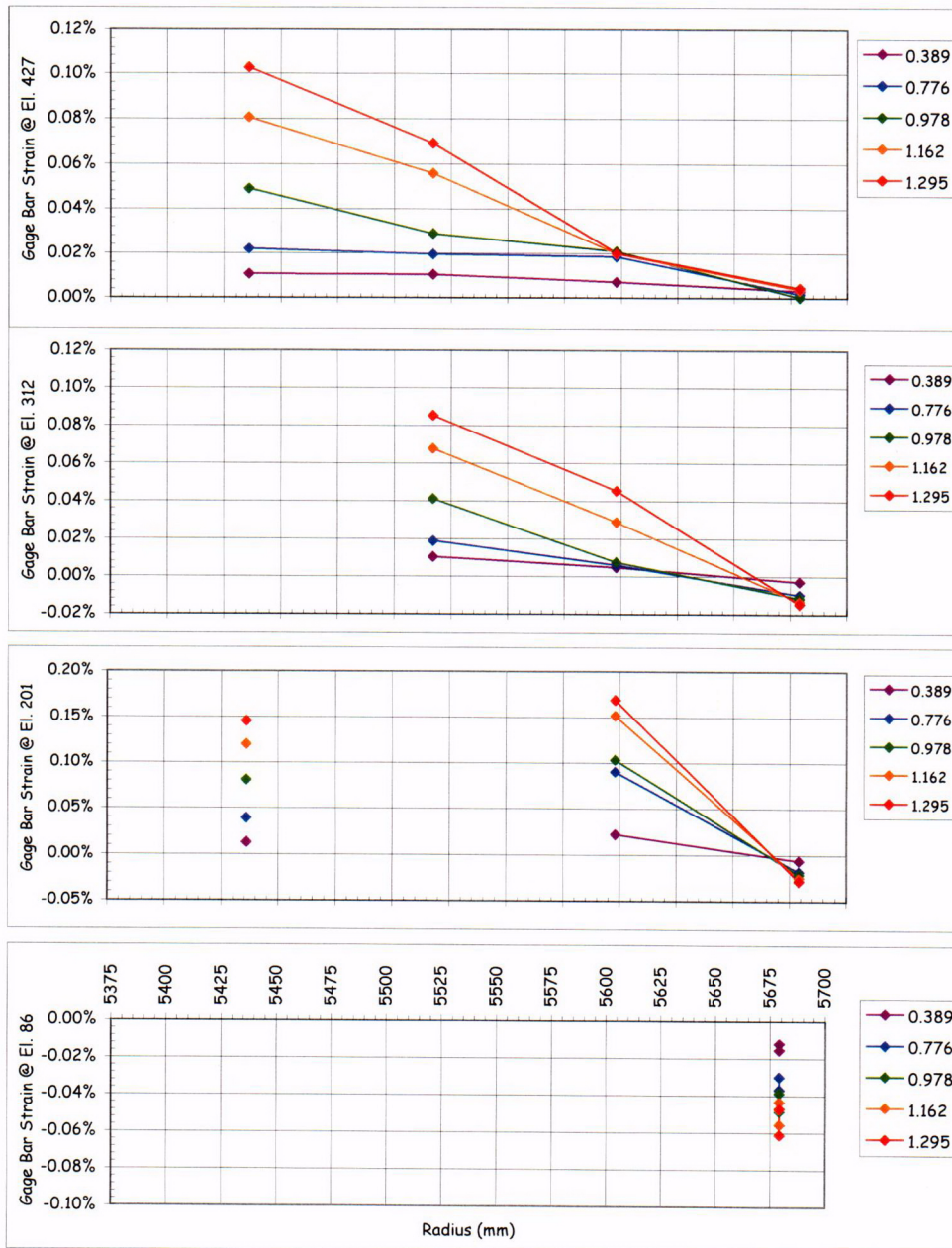


Figure 5.59 LST Gage Bars Strains at Azimuth 135 degrees (due to pressure only)

and 270 degree buttresses. In general, the vertical tendon anchor forces did not exceed the initial tensioning force. The average vertical tendon force at the peak pressure of $3.3P_d$ was 466 kN (104.7 kips) compared to the average tensioning force of 472 kN (106.3 kips). The hoop tendon anchor forces, however, did exceed the initial tensioning force of 424 kN (95.3 kips). The maximum anchor force recorded at the peak pressure of $3.3P_d$ was 550 kN (123.64 kips) for tendon H53. The average anchor force for all the hoop tendons at the peak pressure was 496 kN (111.6 kips). The tendon yield strength (0.2% offset) is approximately 590 kN (132.6 kips), so hoop tendon forces at the anchors were approaching, but had not exceeded their yield strength.

Eight tendons, five hoop tendons (H11, H35, H53, H67, and H68) and three vertical tendons (V37, V46, and V85), were instrumented along their length by placing strain gages on individual strand wires at specified locations. The surviving bonded foil gages are believed to have provided the most reliable data on the strain in the tendons. Figure 5.63 plots the strain history during the LST of the surviving gages on tendon H68. This plot illustrates the variability between strains in different strand wires at roughly the same position along the tendon. Nevertheless, considering an average strain of approximately 0.40% at the start of the LST, the increase in the average strain to 0.80% is nearly identical to the average hoop strain computed from the displacements, at 0.42%.

A more useful way of analyzing the tendon response data is by constructing the tendon force profiles at pressures during the LST, similar to the force profiles constructed for the prestressing loads (see Figures 2.66-2.73). The tendon force profiles for the five instrumented hoop tendons are shown in Figures 5.64 to 5.68. The force profiles include the design and measured values at maximum tension and after seating, and the recorded response during the LST at $0.0P_d$, $1.0P_d$ ($0.389\text{ MPa}/56.4\text{ psi}$), $2.0P_d$ ($0.776\text{ MPa}/112.5\text{ psi}$), $2.5P_d$ ($0.978\text{ MPa}/141.8\text{ psi}$), $3.0P_d$ ($1.162\text{ MPa}/168.5\text{ psi}$), and at the maximum pressure, $3.3P_d$ ($1.295\text{ MPa}/187.8\text{ psi}$). The profiles are also shown during depressurization at approximately $2.5P_d$, $2.0P_d$, $1.0P_d$, and $0.0P_d$. These force profiles were constructed by converting the average strain from all the foil strain gages at a given position to a force using the actual tendon force-strain test data and combining the computed forces with load cell data. When only a single strain gage survived at a given position, it is noted on the profile.

There is not adequate data to assume the shape of the hoop tendon force profile between the surviving measurement positions, so only the force at the measurement locations are shown. There is enough data to suggest, however, that the tendon force distribution tends to become more uniform, with the largest increase in strain occurring near the mid-point of the tendon, where the initial prestressing force was the smallest. This may be due to a combination of local yielding and/or slipping as the tendons try to maintain equilibrium and local deformation of the cylinder wall. Comparing the differential strain at the midpoint of the tendons to the hoop strain calculated from the wall displacement at that location (see Figures 5.66 and 5.67) indicates that the tendon strain is greater than what would be expected if the tendon did not slip relative to the wall. After unloading, however, the initial tendon force profile (at the start of the LST) is almost completely recovered, which implies that any redistribution occurring during the LST is entirely elastic. This is not a completely satisfying observation, since it would seem likely that any redistribution of tendon forces due to slipping would remain after depressurizing. This reinforces the observation that the change in tendon forces is also due to the local elastic deformation of the wall.

The force profiles for the vertical tendons, constructed in the same manner as the hoop tendon profiles, are shown in Figures 5.69 to 5.71. Again, since the gage mortality was lower for the vertical tendons than the hoop tendons and the force profile is more nearly a continuous function, curves were fit through the data to facilitate interpretation and comparison of the data with the design assumptions. The data again shows that the vertical tendon force distribution becomes more uniform as the pressure increases, and the largest relative increase occurs at the mid-point of the tendon, i.e. the apex, for the vertical tendons. This suggests that the tendons must slip relative to the concrete wall to allow the forces to redistribute; however, as with the hoop tendons, recovery of the initial tendon force distribution is nearly complete after depressurization. In this case, however, it is difficult to argue that the tendon force distribution is dominated by the local radial deformation of the concrete wall/dome, since those in the dome are much smaller than those in the cylinder wall, which is inconsistent with the observed change in the force distribution.

While the tendon response measurements provided new insight into the behavior of unbonded tendons under limit load conditions, some apparent paradoxes were identified that might be answered by further testing and analysis. One conclusion is apparent and undeniable, however. The change in tendon anchor forces is not a reliable indicator, by itself, of the change in force along the length of the tendons, and any attempts to preclude tendon rupture by measuring only the anchor force will not be adequate.

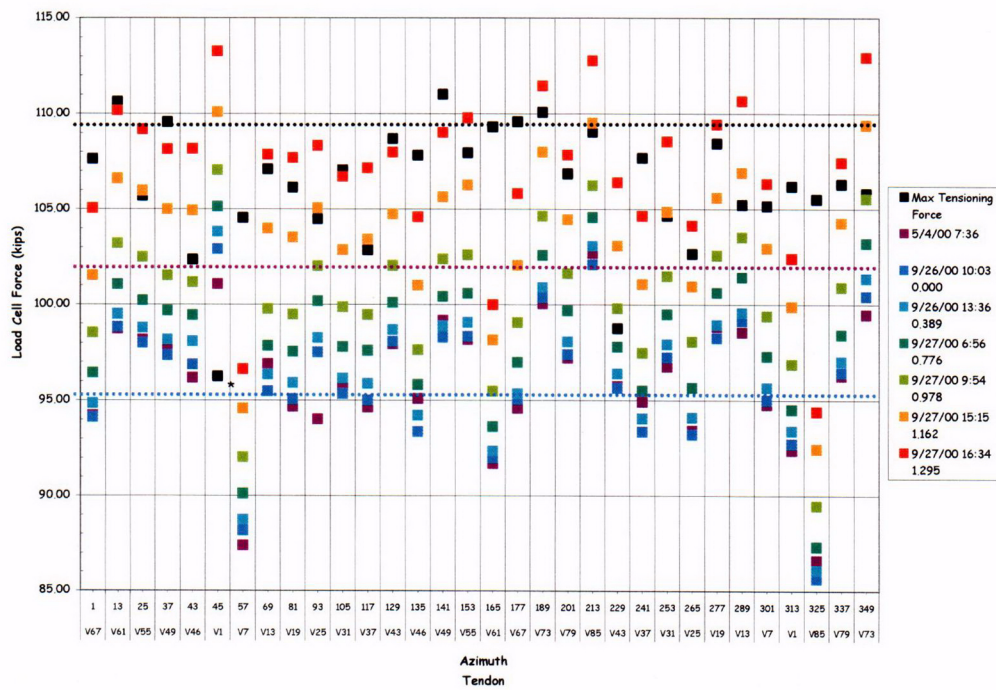


Figure 5.60 LST - Vertical Load Cells

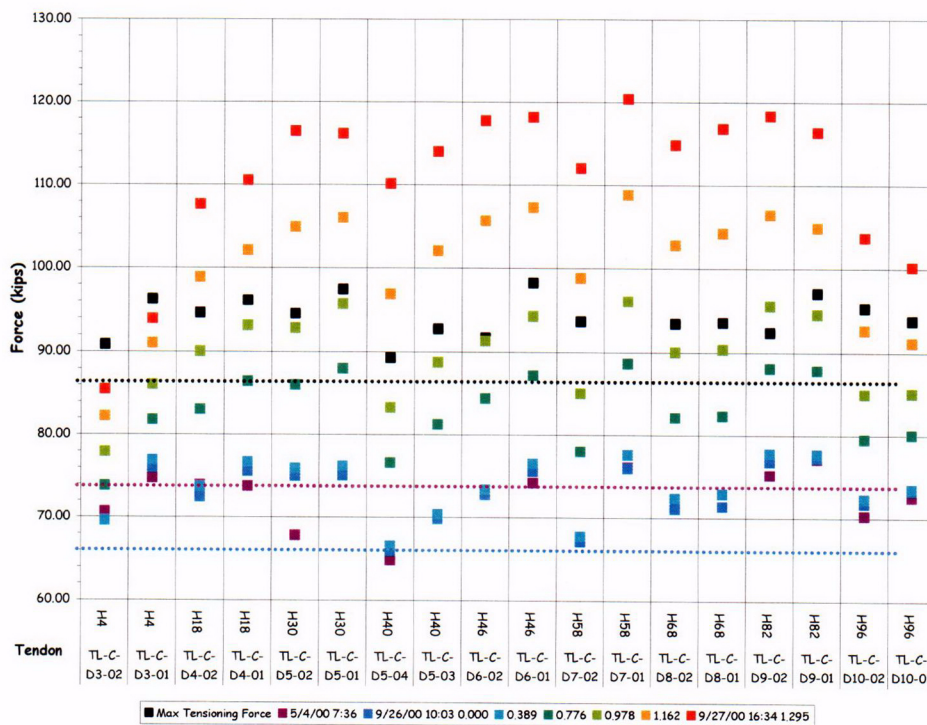


Figure 5.61 LST - Hoop Load Cells at 90 degrees

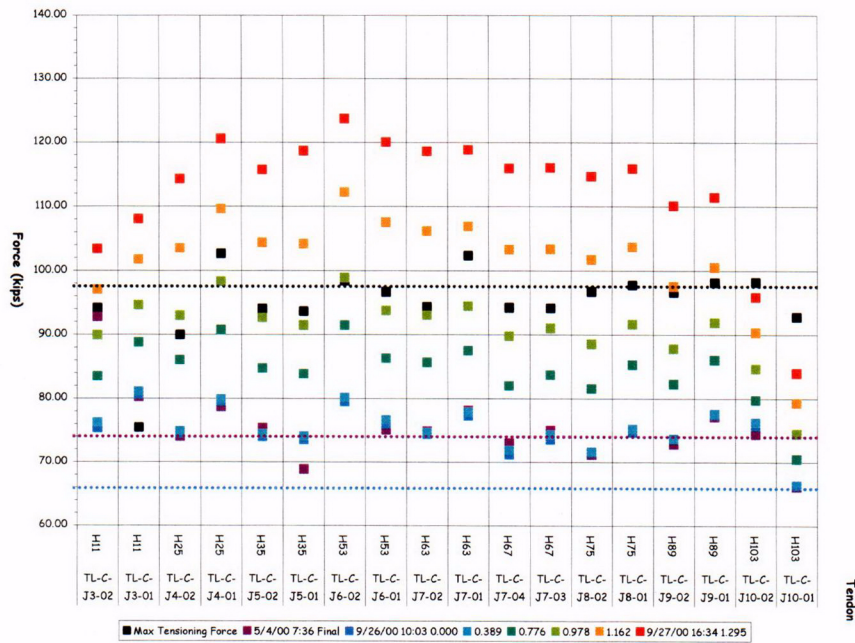


Figure 5.62 LST - Hoop Load Cells at 270 degrees

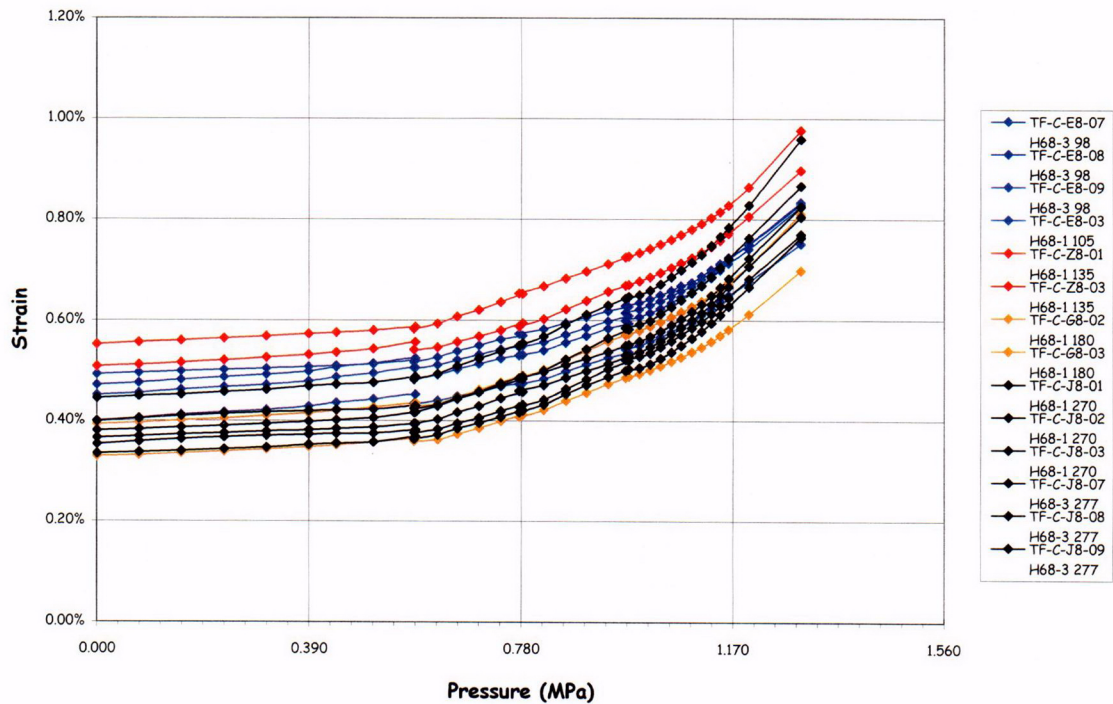


Figure 5.63 LST - H68 Tendon Strains

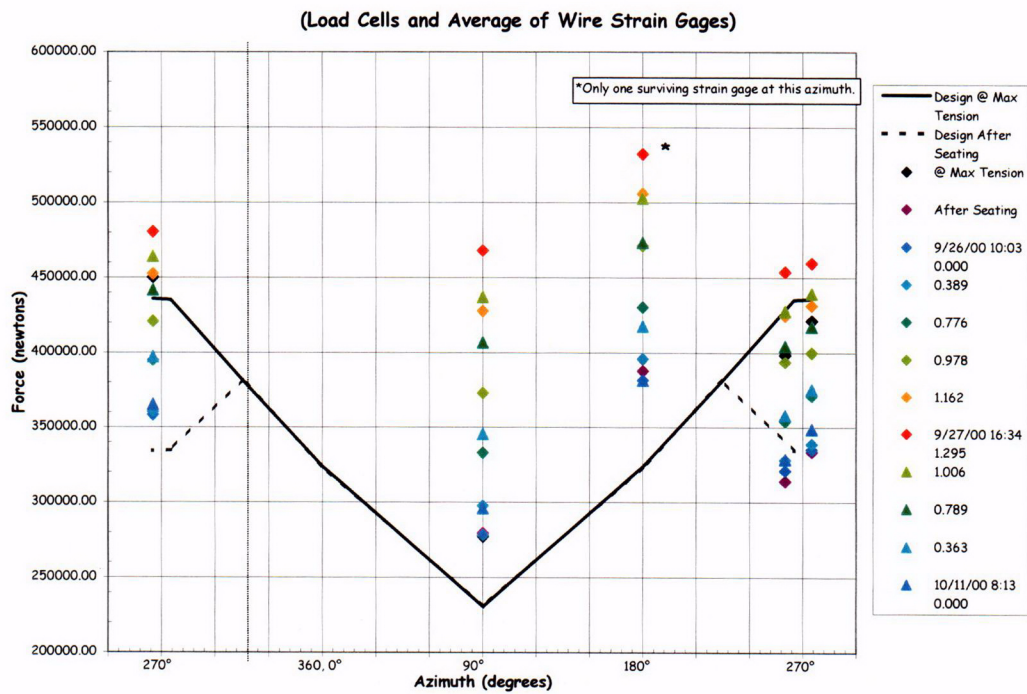


Figure 5.64 H11 Tendon Force Distribution, El. 1854

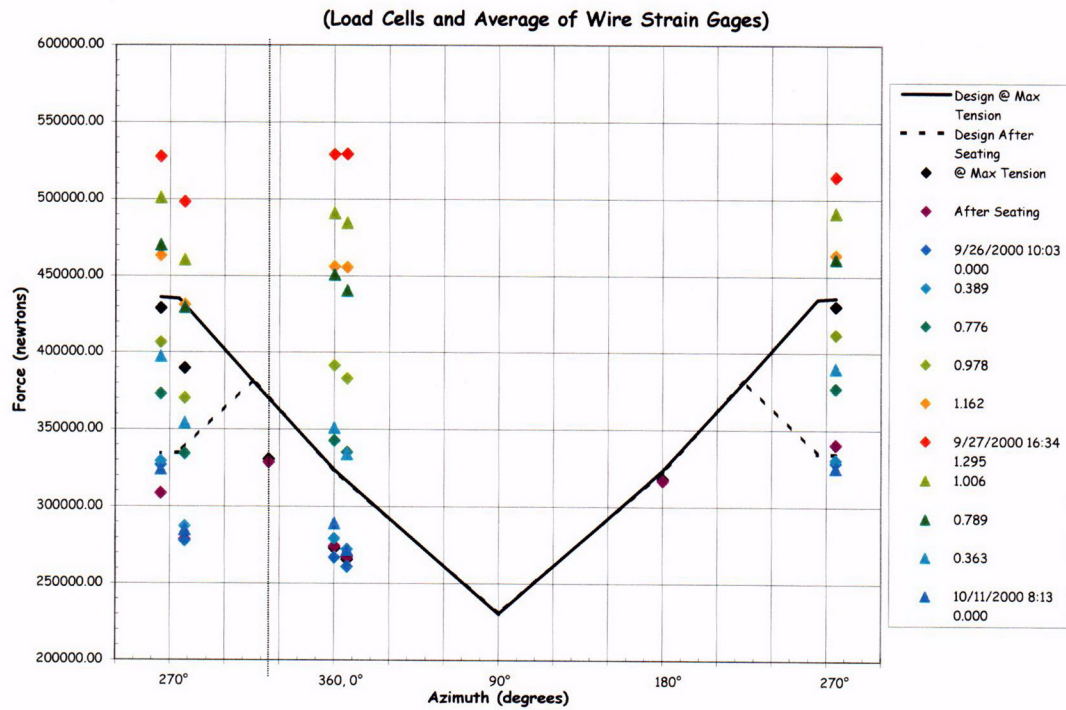


Figure 5.65 H35 Tendon Force Distribution, Elev. 4572

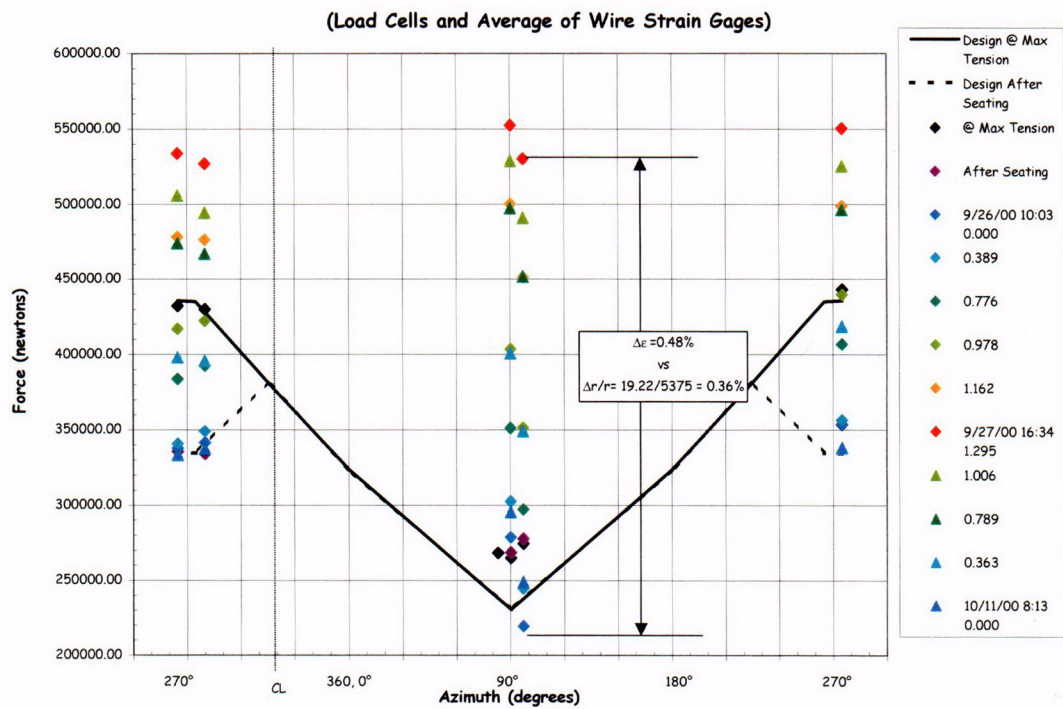


Figure 5.66 H53 Tendon Force Distribution, Elev. 6579

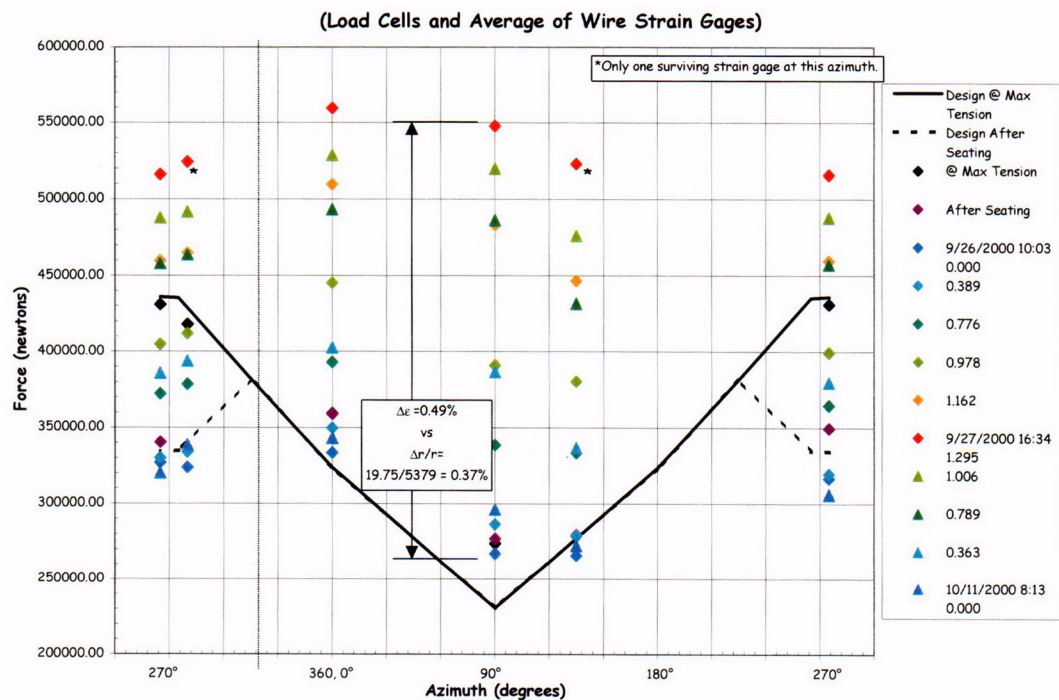


Figure 5.67 H67 Tendon Force Distribution, Elev. 8153

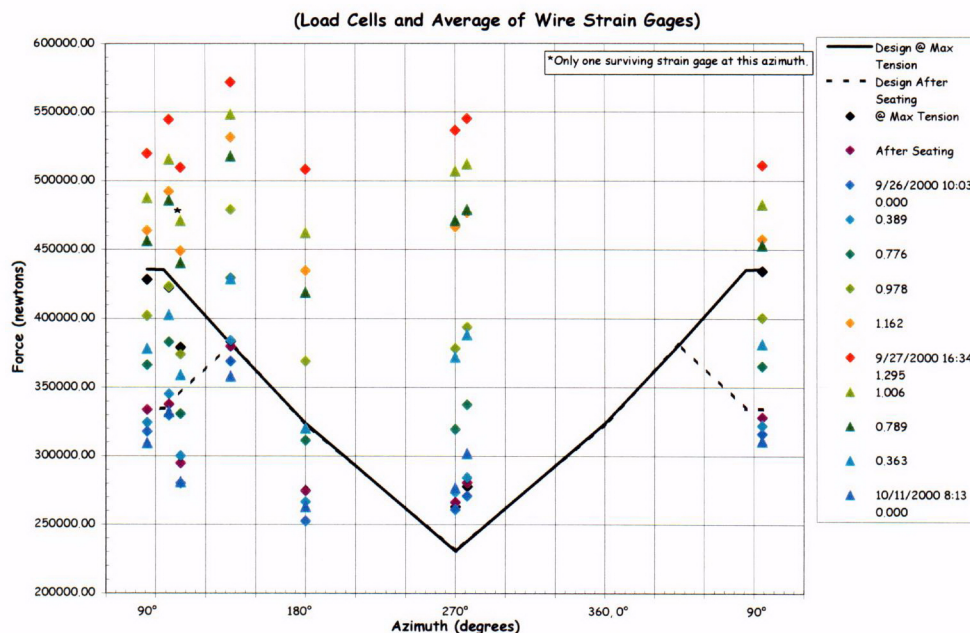


Figure 5.68 H68 Tendon Force Distribution, Elev. 8280

5.3.2.1.5 Acoustic Response

The complete reports from the Acoustic System Operator, Pure Technologies, are provided in Appendix K. As stated in Section 3.2.8, the objectives for the acoustic system were to detect tendon or rebar breaks, concrete cracking or crushing, and liner tearing/leakage. The acoustic system response data, which helped to identify when the PCCV model began leaking, was described in Section 5.2.2 (see Figure 5.17).

There were no tendon wire or rebar breaks during the LST; however, events defined as tendon ‘pings’ were reported. These tendon pings were interpreted as a readjustment or reseating of the tendon wires/strands as they were tensioned, but the magnitude of these acoustic events are much lower than those associated with a wire break. Figure 5.72 shows the location of the tendon pings are concentrated at the buttresses. Whether this is indicative of source of these events or merely reflects that any tendon events will be transmitted more rapidly along the tendon strands to the acoustic sensors on the buttresses is speculative, but reasonable. A histogram of the tendon ping events as a function of pressure is shown in Figure 5.73. The fact that the majority of tendon pings occurred around $2.0P_d$ is noteworthy, but the reason for physical significance of this is not obvious. It may be that a certain level of tension must be applied to reseal the strands, or it may simply be that this pressure was held for almost eight hours and the number of events that accumulated at this time appears to be significant.

A total of 489 cracking events were detected from March 3 to September 27, 2000. Two-hundred twenty nine of these events were recorded during the LST. These cracking events represent distinct acoustic events, as distinguished from the ubiquitous ‘crackling’ which occurred nearly continuously during the period the PCCV was monitored by the acoustic system. This crackling is believed to be the acoustic manifestation of microcracking and shearing in response to environmental and pressure loading. The acoustic events identified as cracking represent the formation or extension of discrete macrocracks in response to the applied pressure or other loads. Figure 5.74 maps the location of the cracking events during the LST, grouped by pressure bands. No obvious pattern emerges from this map except that the majority of cracks occurred in the middle section of the cylinder wall, where the strains and displacements were greatest. A histogram of the cracking events as a function of pressure, shown in Figure 5.75, however, reveals the majority of cracking events occurring in the range of 1.5 to $2.0P_d$ where the initial loss of stiffness, presumed to be due to concrete cracking, was already noted.

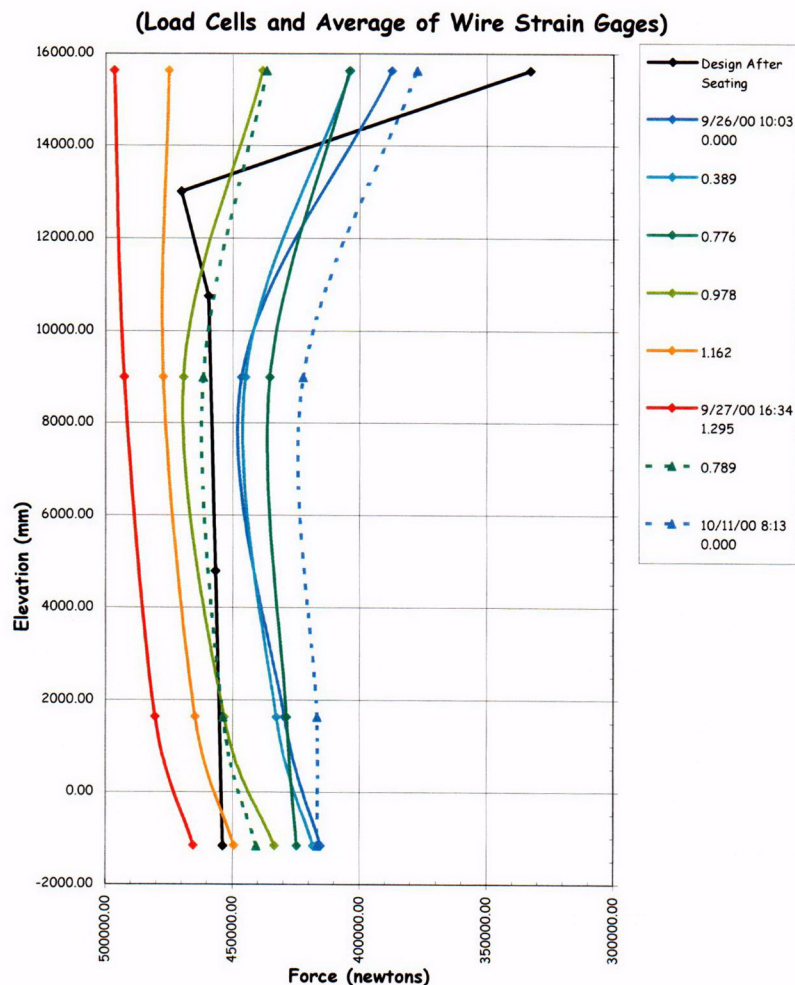


Figure 5.69 V37 Tendon Force Distribution, Azimuth 240 degrees

5.3.2.2 Posttest Inspection

Post-LST inspection of the PCCV model consisted of external crack mapping, visual inspection of the liner and metallurgical examination of the liner tears, and posttest measurements around the E/H.

5.3.2.2.1 Crack Mapping

New cracks and extensions of existing cracks within the crack mapping zones resulting from the LST (see Fig. 5.8) were traced in red and the surface was photographed to document the crack locations (e.g. Fig 5.22). The cracks were then transferred to the crack map drawing, shown in Figure 5.76, which shows all the major cracks identified after various loading stages. In general, concrete cracking was not extensive or very severe, with the exception of some areas around the E/H and some of the smaller penetrations. As noted in Chapter 3, there was no effort to measure crack widths. While it can be observed that some of the larger cracks around the E/H are near the liner tear locations, there was no further effort to correlate the crack locations with other events or data.

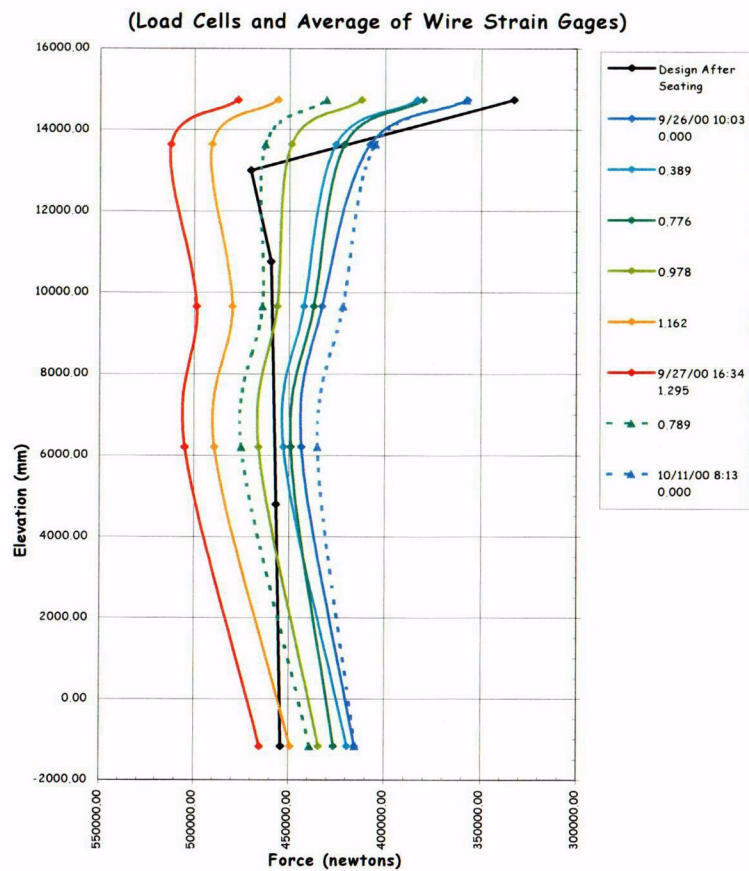


Figure 5.70 V46 Tendon Force Distribution, Azimuth 135 degrees

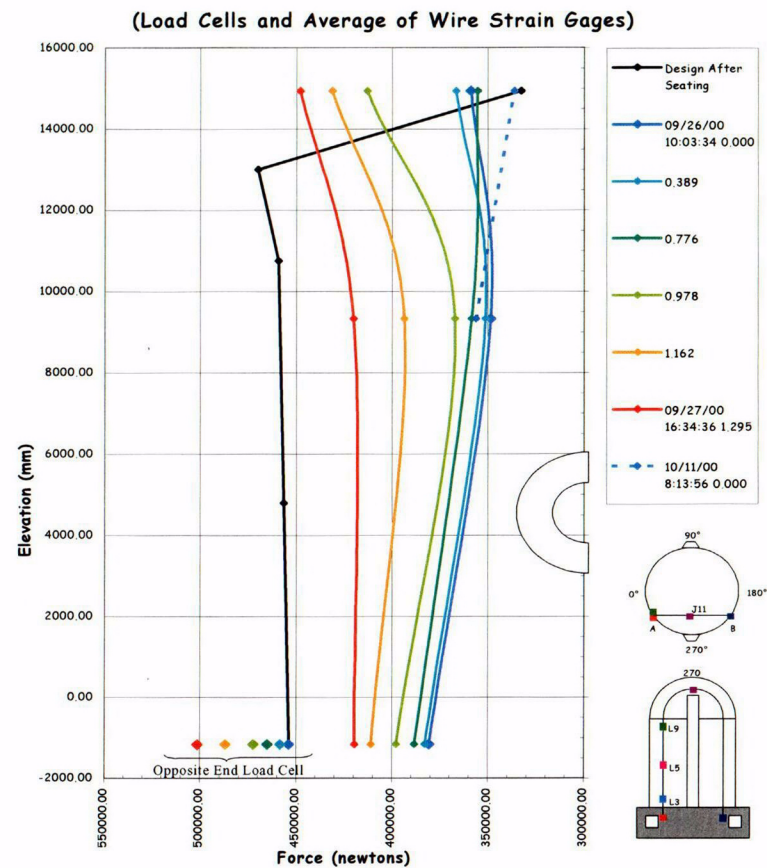


Figure 5.71 V85 Tendon Force Distribution, Azimuth 325 degrees

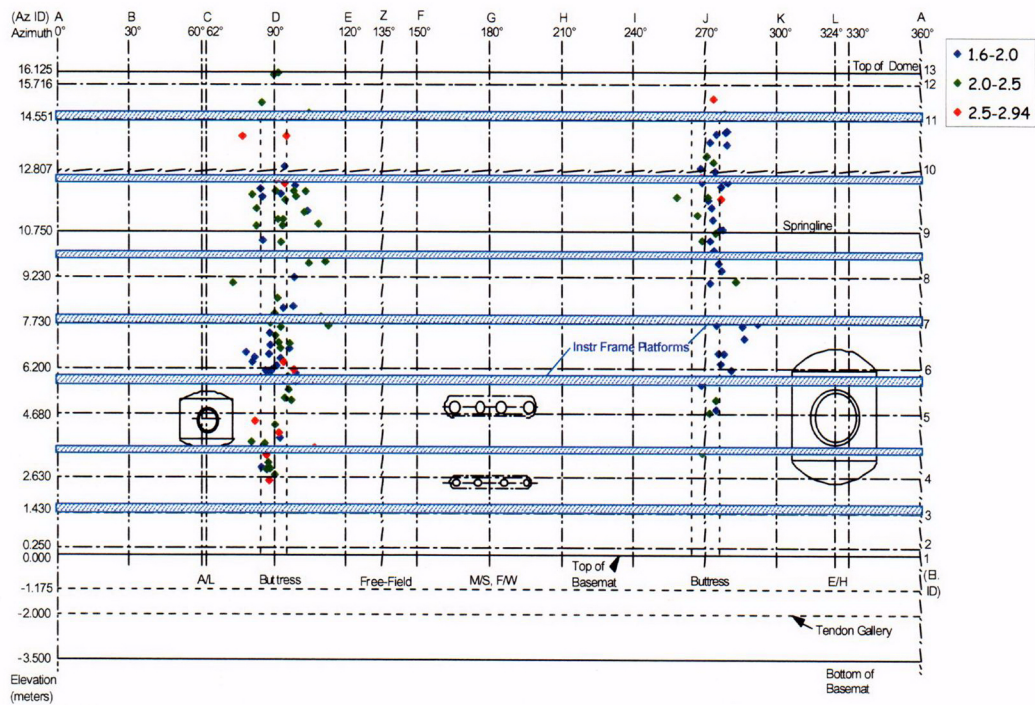


Figure 5.72 LST – Tendon Ping Acoustic Events

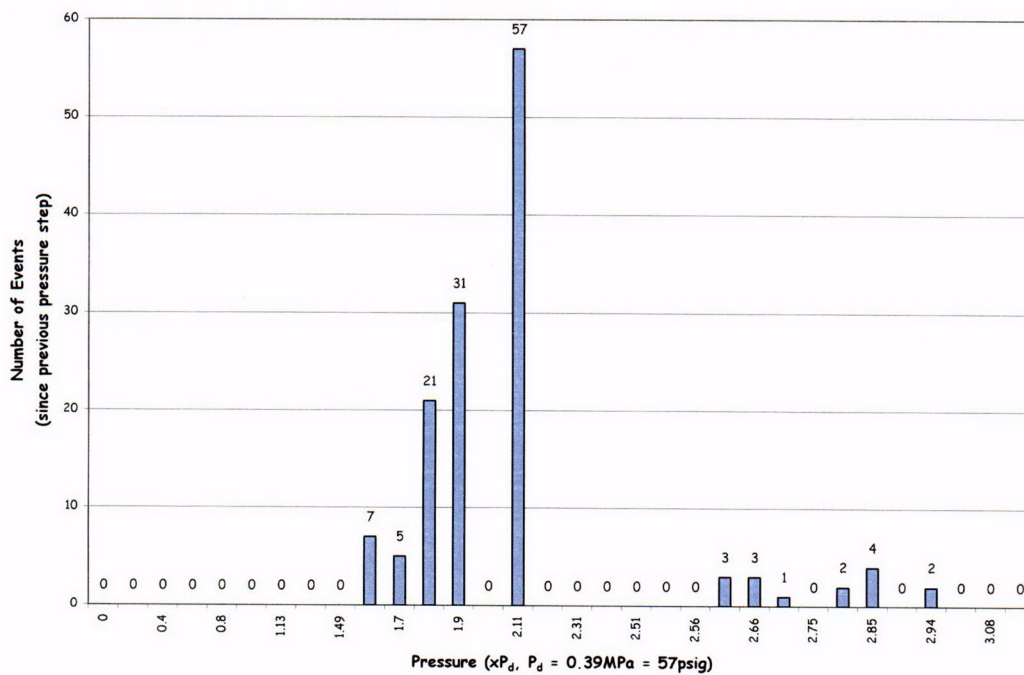


Figure 5.73 LST – Tendon Ping Event vs. Pressure Histogram

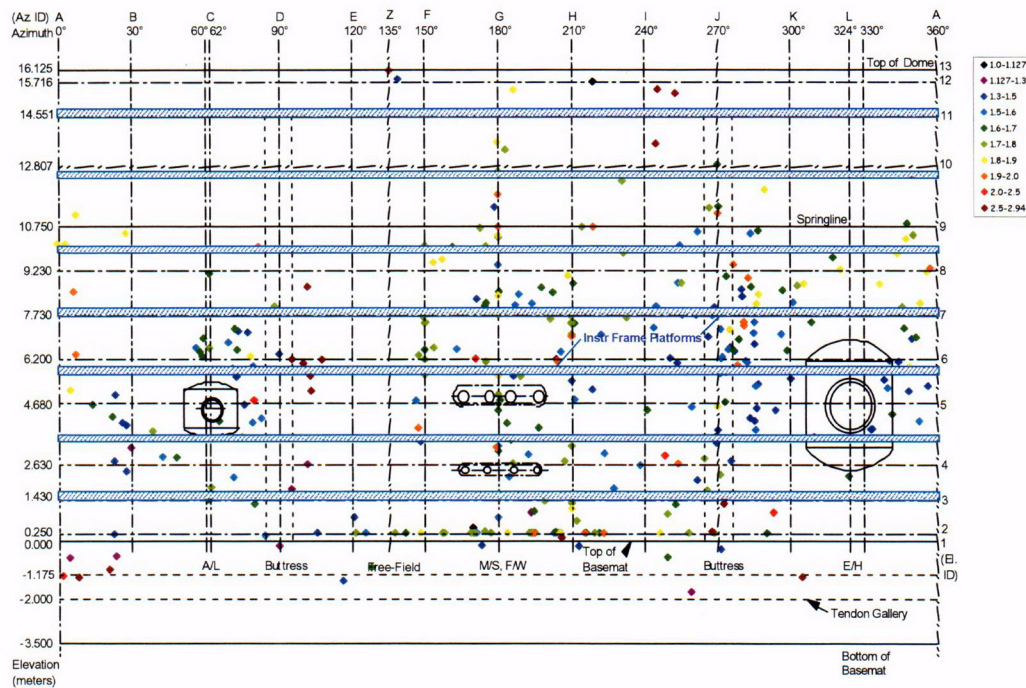


Figure 5.74 LST – Concrete Cracking Acoustic Events

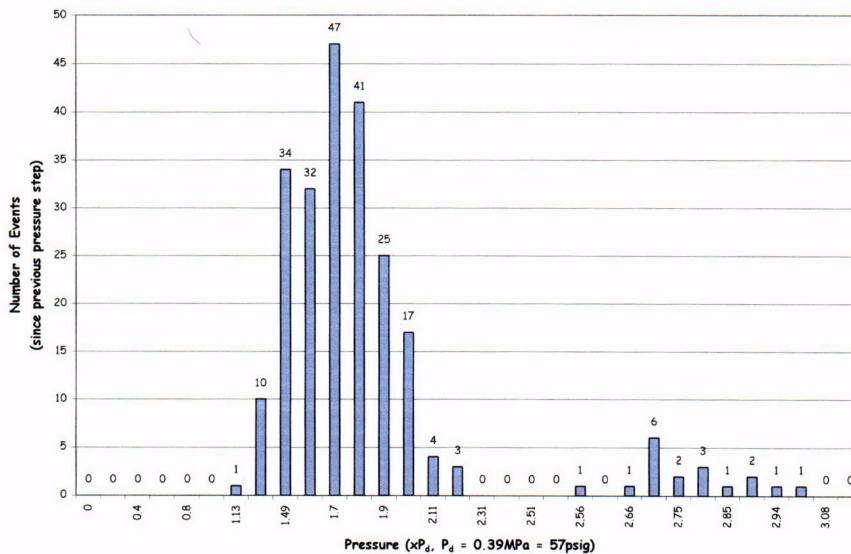


Figure 5.75 LST – Concrete Cracking Events vs. Pressure Histogram

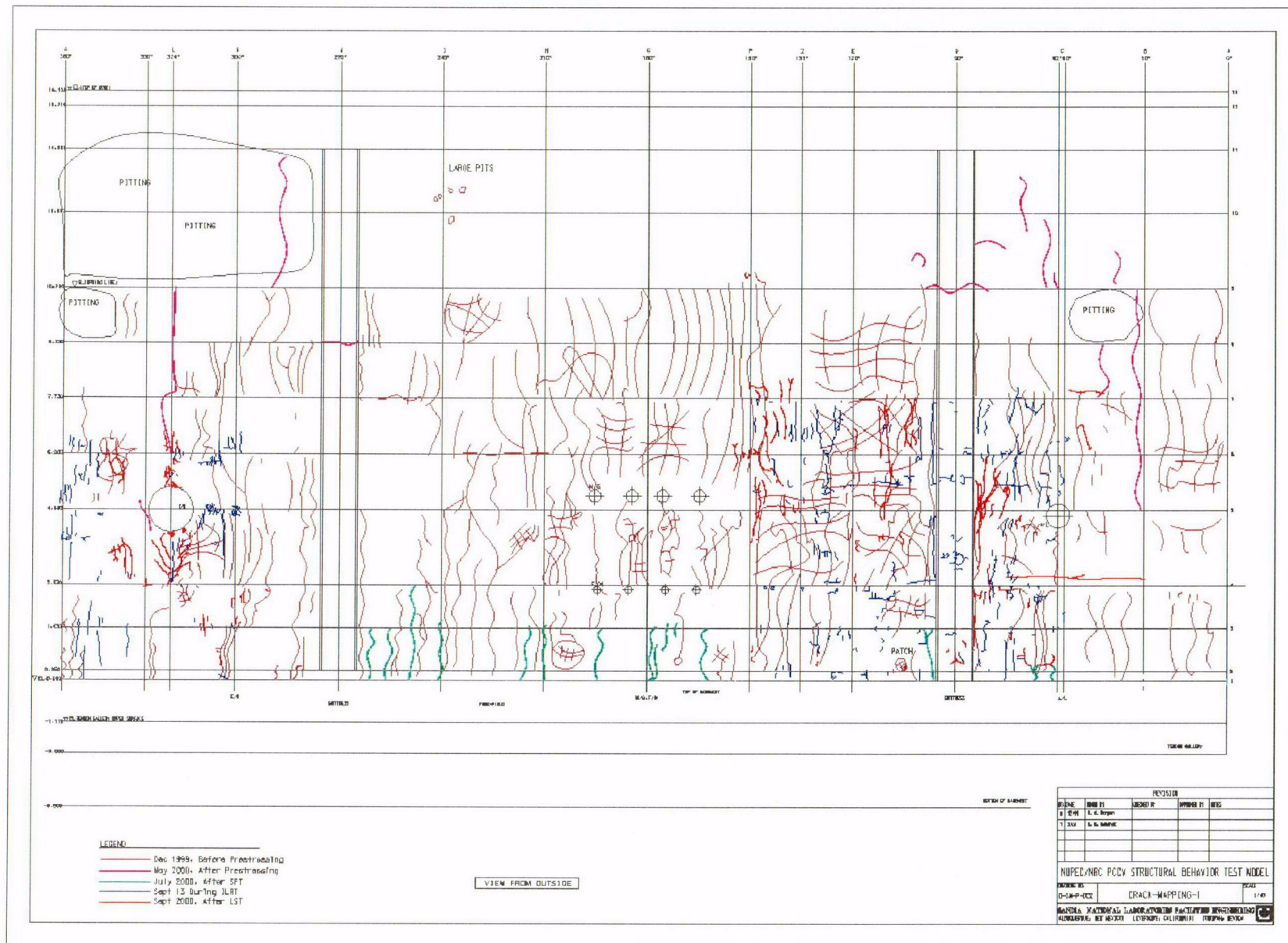


Figure 5.76 Post-LST Concrete Crack Map

5.3.2.2.2 Liner Inspection

As noted in Section 5.2.3, after entering the model following the LST, the liner surface was examined carefully and 26 discrete tears were found at 18 different locations, the grouping by location being somewhat arbitrary. The location of the tears are mapped in Figure 5.77. The location numbers are subsequently used to identify the tears.

One immediate observation was that each liner tear was at or very near a field weld seam in the liner. No tears were found in the undisturbed parent material or at a shop weld.

The acoustic events, later associated with the sound of the nitrogen gas escaping through the liner tears, are superimposed on the tear map in Figure 5.78, along with the approximate pressure levels when these events were first detected. The first tearing event appears to be clearly associated with the tears along the edge of the E/H embossment (#7, #12, #13, and #15), although it is arguable which of these occurred first. The other acoustic tearing events cannot be as clearly identified with any specific tear or tears, and, near the end of the test, it may have been difficult to distinguish the separate 'tearing' events from each other since gas continued to escape through each tear after it occurred.

A typical liner tear (#2) as it appeared during the initial inspection is shown in Figure 5.79. In addition to the liner tears, a pattern of buckling appeared throughout the middle section of the cylinder wall. The buckling pattern, also illustrated in Figure 5.79, is believed to have occurred during depressurization, when the permanently stretched liner could not accommodate the elastic recovery of the cylinder wall.

After the initial inspection of the liner, a more methodical inspection was undertaken. Each tear was photographed and matched with photographs of the 'backside' of the liner before the concrete was placed. (One early program decision was to photograph the entire length of every field weld made during the fabrication of the liner. While this was a very time-consuming and painstaking task, the benefit obtained in understanding the causes of the liner tearing was worth the effort.) A sample of the pre-LST exterior condition compared to the post-LST interior condition for Tears #7, #12, #13 and #15 at the E/H, #2 at a free-field weld seam, and #16 at a 'rathole' detail are shown in Figures 5.80 to 5.85.

The paint was then removed from each tear, allowing the liner tear to be seen without being obscured by the paint. Each tear was then photographed again for documentation. Figure 5.86 shows an close-up of Tear #13 after removing the paint. With the paint removed, it was clear that the weld was repaired or had been reworked by grinding at nearly every tear. Note the grind marks in Figure 5.86, which occurred during erection and welding of the liner. (The paint was removed by using chemical strippers; no paint was removed by mechanical methods.)

While this initial inspection was being completed, a detailed posttest liner inspection plan was being developed. After reviewing the plan with NUPEC and the NRC, the plan, consisting of the following elements, was implemented.

1. In-situ examination:
 - a. In addition to the visual/photographic records, ultrasonic thickness measurements were made at each tear location and at several baseline locations where tears did not occur.
2. Destructive examination:
 - a. Twenty-five liner specimens were removed from the model (see Figures 5.87 and 5.88).
 - b. Eighteen of the liner specimens were subjected to metallographic analysis.
 - c. Sample weld specimens were subjected to metallographic analysis.
 - d. After the liner specimens were examined by SNL, the unused portions were sent to NUPEC for further examination. The results of NUPEC's examination have been reported separately.

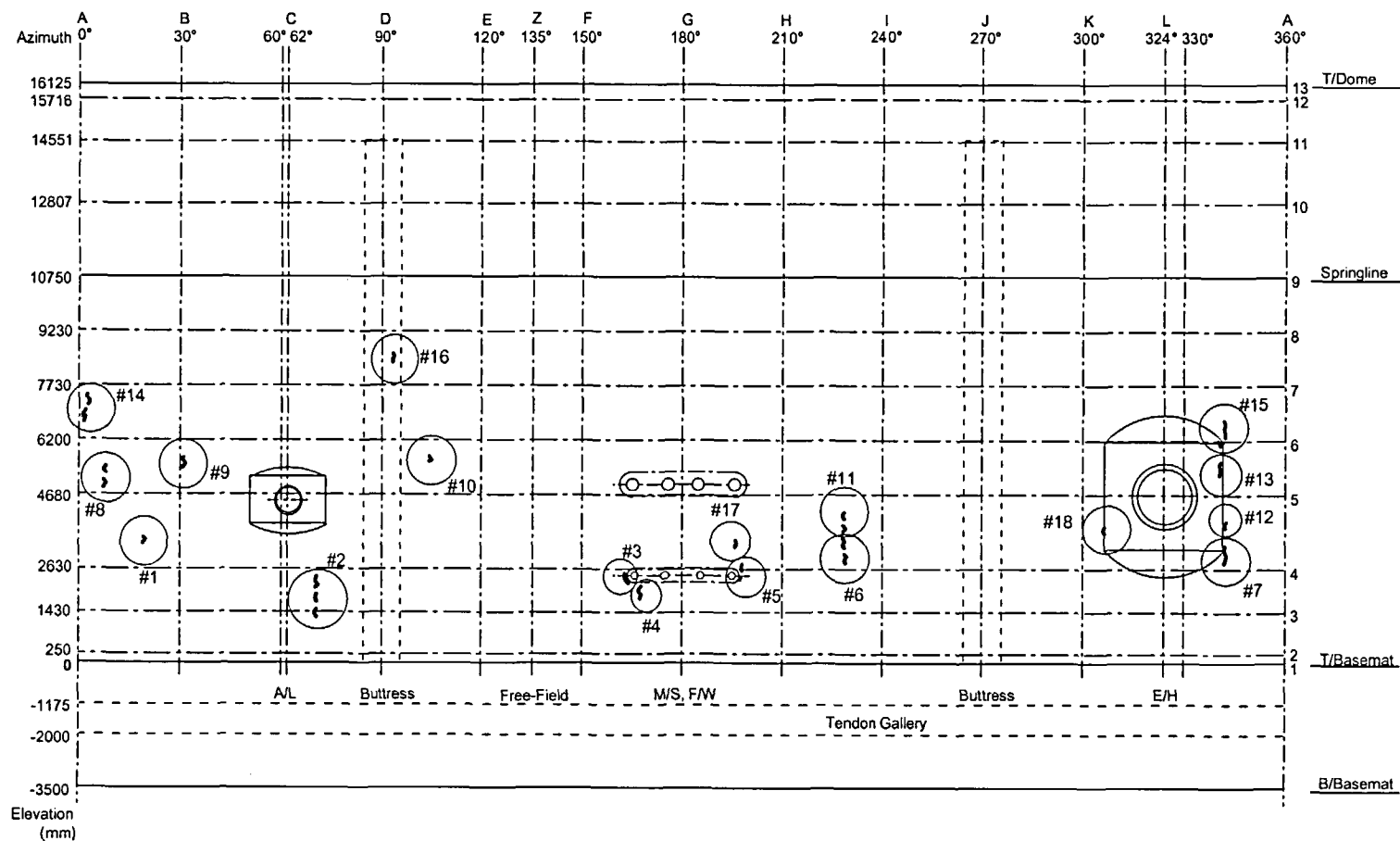
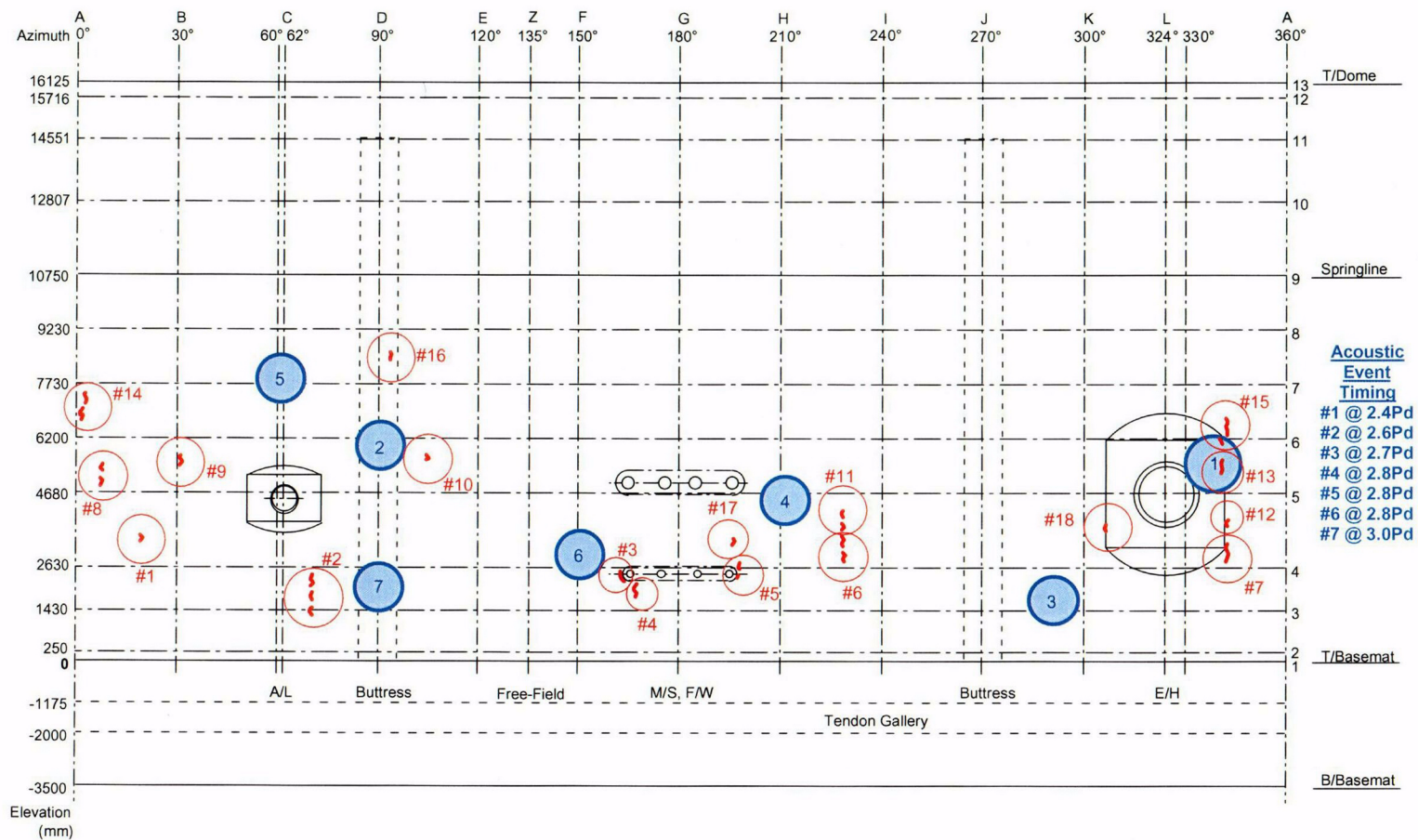


Figure 5.77 Post-LST Liner Tears



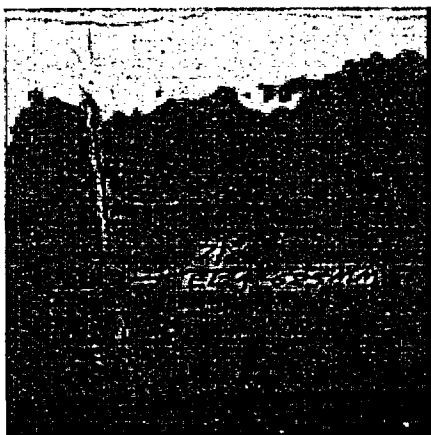


Figure 5.79 Post-LST Liner Tear (#2) and Liner Buckling

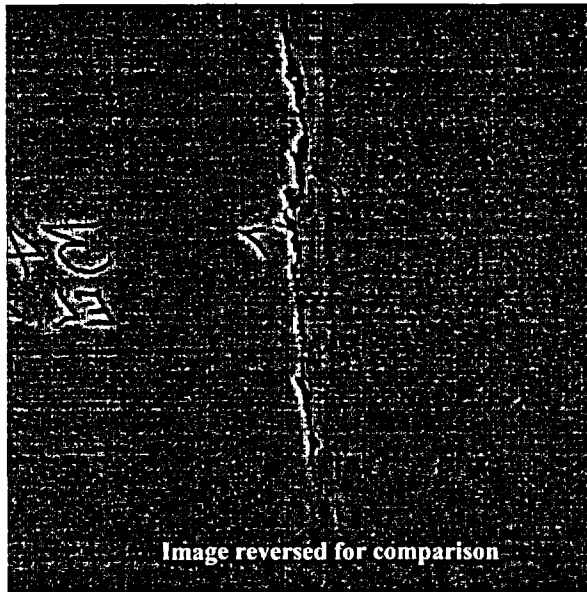


Image reversed for comparison

Figure 5.80 Tear #7 at E/H

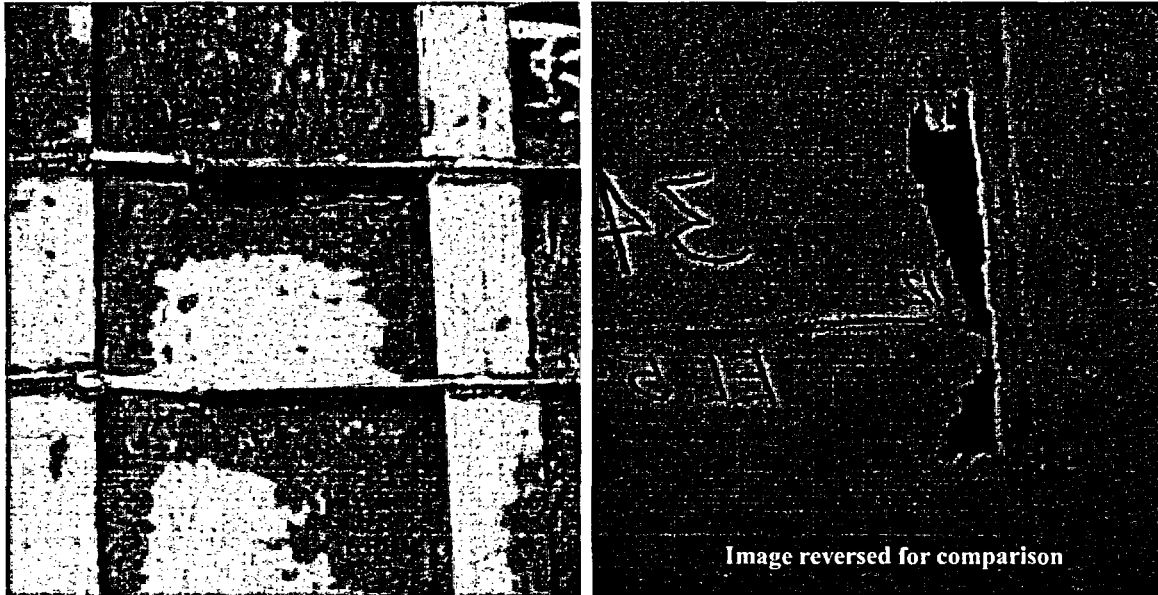


Figure 5.81 Tear #12 at E/H

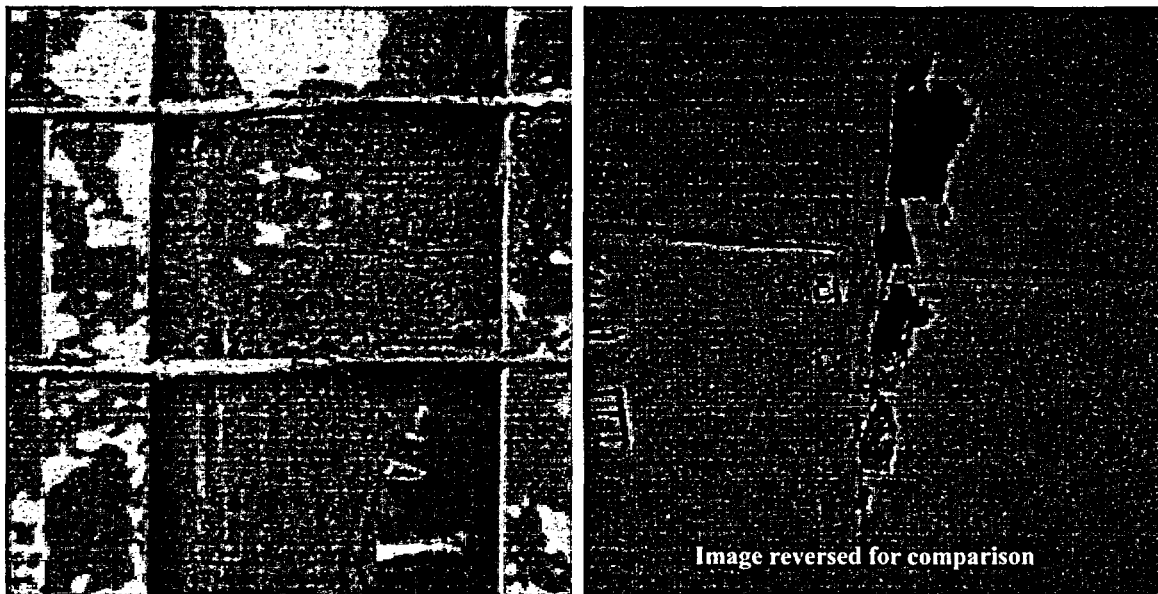


Figure 5.82 Tear #13 at E/H

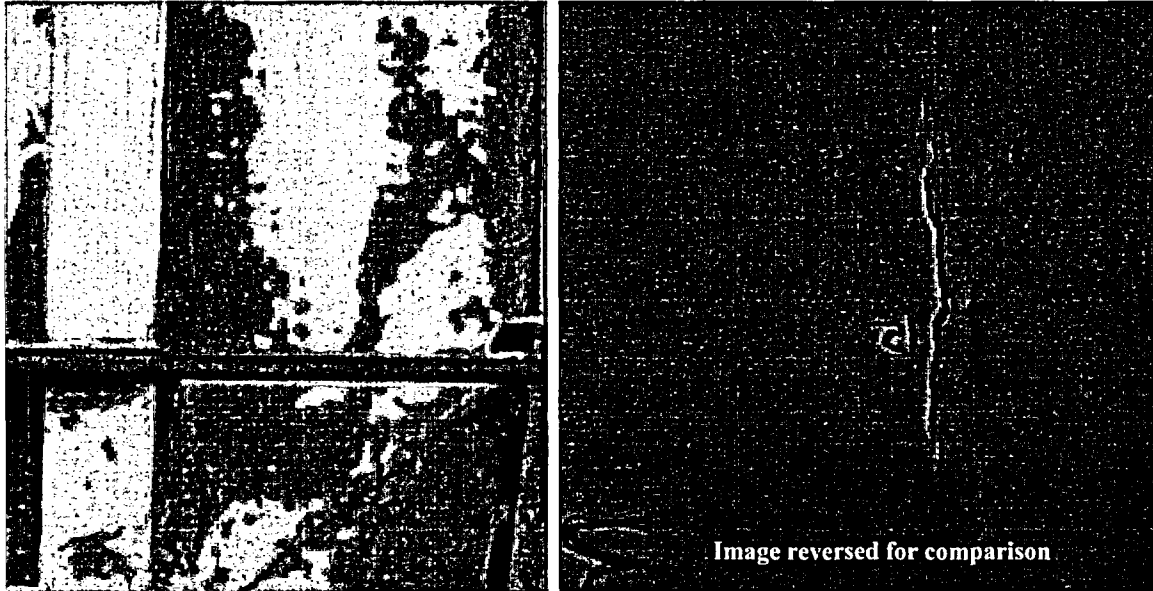


Figure 5.83 Tear #15 at E/H



Figure 5.84 Tear #2, Free-Field

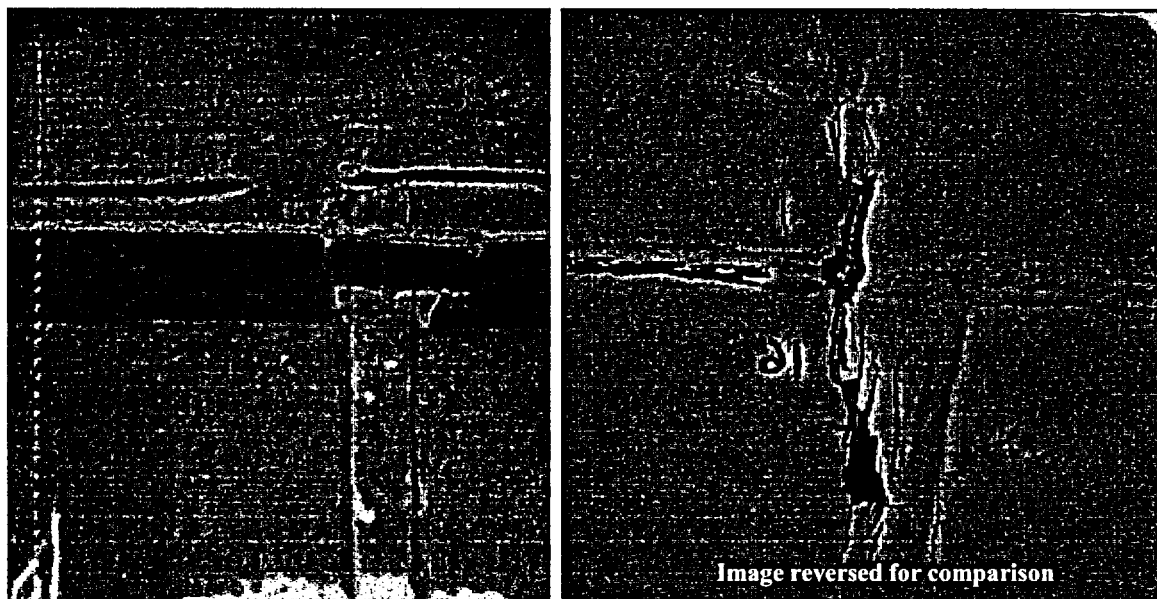


Figure 5.85 Tear #16 at Rathole Detail

The results of the liner inspection are detailed in Appendix L. The conclusions of the inspection and metallographic analysis are repeated below.

1. Nearly all of the tears occurred in areas where the liner thickness was reduced ~25% or more by grinding done in association with repair welding. Extensive localized plastic deformation culminating in ductile tearing occurred in these thinned areas as the structure was being tested. This appears to have been the most prevalent cause of liner failure.
2. In samples where quantification was possible, it appears that the reduced thickness at the point of failure was up to 50% of the local material thickness.
3. At the E/H
 - a. #15: 50%-60% reduction by grinding
 - b. #13: 25% reduction by grinding
 - c. #12: >10% reduction by grinding
 - d. #7: 25% reduction by grinding
4. @ the Free-Field
 - a. #16-1 (D7): no tear, no repair ~10% reduction in thickness (post-LST)
 - b. #16-2: tear, single weld repair, thickness reduction on both sides of weld
5. Geometric features may also have contributed to the formation of some tears. These include structural transitions, such as those at the feedwater penetration and the equipment hatch transition boundaries, discontinuities in horizontal stiffeners, and discontinuities in weld back-up bars. A missing segment in a horizontal back-up bar appears to have been primarily responsible for one tear (#16).
6. Only one tear occurred in association with a material or weld defect. A lack-of fusion weld defect was found at the initiation site of tear #1.
7. The specially produced quarter-scale liner material exhibited mechanical properties that may have made it particularly prone to plastic strain localization and tearing. While nearly conforming to the specifications for full-thickness material, the quarter-thickness plate exhibited a yield strength much higher than the specified minimum (383 MPa compared with 225 MPa) and an unusually high yield-to-ultimate-strength (YS/UTS) ratio (0.77). This high YS/UTS ratio is qualitatively consistent with extensive localized plastic strain culminating in ductile tearing in regions where more than ~25% of the liner thickness had been ground off, as was observed near most of the tears.

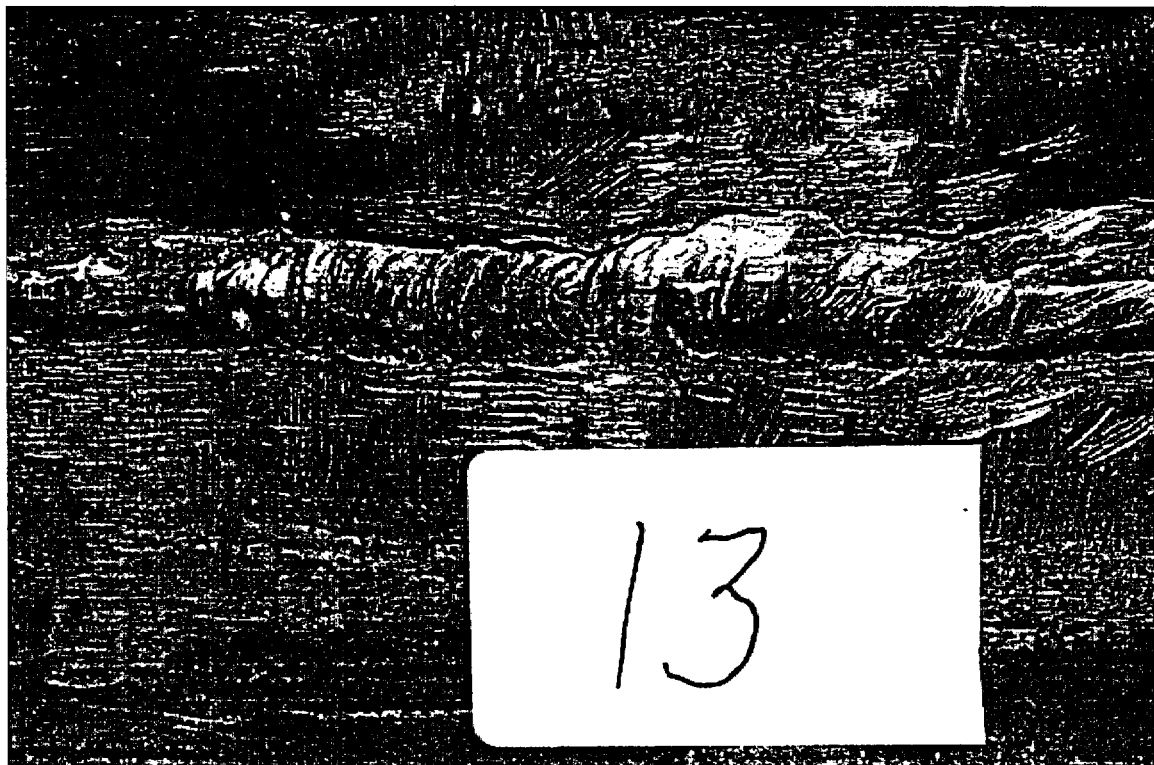


Figure 5.86 Close-Up of Tear #13 after Removal of Paint

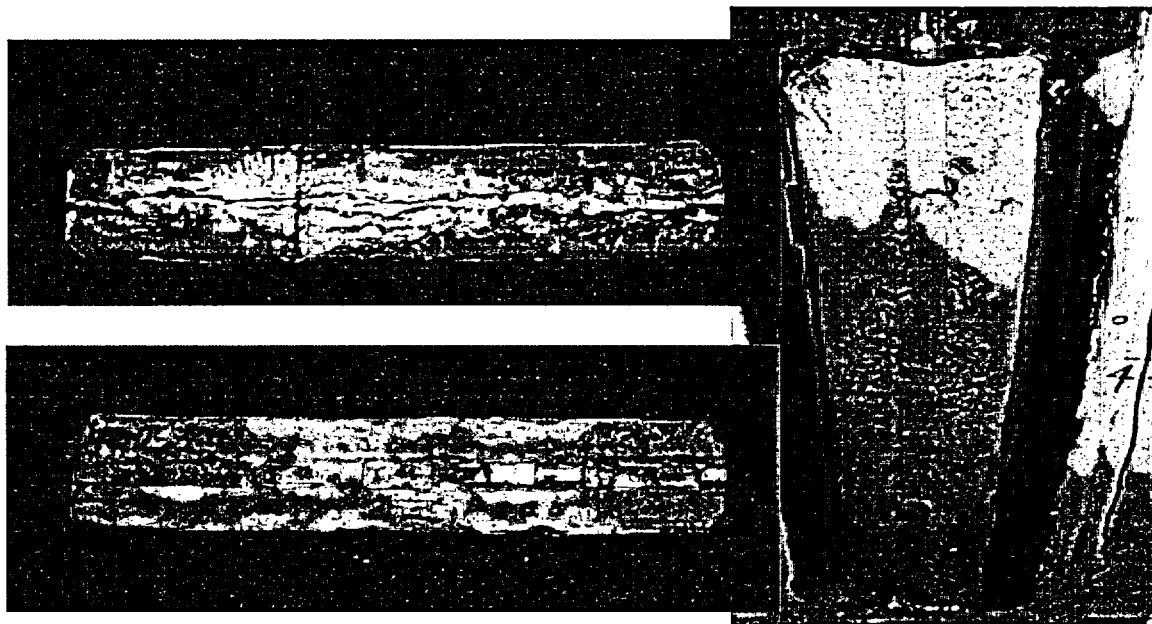


Figure 5.87 Liner Specimen at Tear #2